

CLIMATE VARIABILITY AND CALIFORNIA LOW-LEVEL TEMPERATURE INVERSIONS

A Paper From:

California Climate Change Center

Prepared By:

**Sam F. Iacobellis, Joel R. Norris, Masao
Kanamitsu, Mary Tyree, and Daniel R.
Cayan
Scripps Institution of Oceanography**

DISCLAIMER

This paper was prepared as the result of work sponsored by the California Energy Commission (Energy Commission) and the California Environmental Protection Agency (Cal/EPA). It does not necessarily represent the views of the Energy Commission, Cal/EPA, their employees, or the State of California. The Energy Commission, Cal/EPA, the State of California, their employees, contractors, and subcontractors make no warrant, express or implied, and assume no legal liability for the information in this paper; nor does any party represent that the uses of this information will not infringe upon privately owned rights. This paper has not been approved or disapproved by the California Energy Commission or Cal/EPA, nor has the California Energy Commission or Cal/EPA passed upon the accuracy or adequacy of the information in this paper.



Arnold Schwarzenegger, *Governor*



DRAFT PAPER

March 2009
CEC-500-2009-020-D

Acknowledgments

Support for this research was provided by the State of California through the California Air Resources Board and the California Energy Commission Public Interest Energy Research Program and by the National Oceanic and Atmospheric Administration (NOAA) Regional Integrated Sciences and Assessments Program through the California Applications Center. National Centers for Environmental Prediction Reanalysis data was provided by NOAA through their website at www.cdc.noaa.gov/. Radiosonde data was obtained from the Earth System Research Laboratory through their website at <http://raob.fsl.noaa.gov/>. Surface temperature data was obtained from the NOAA National Climatic Data Center (NCDC) at www.ncdc.noaa.gov/oa/climate/ghcn-monthly/index.php and <http://cdo.ncdc.noaa.gov/CDO/cdo>. Adjusted radiosonde data sets were provided by the Universitat Wien at www.univie.ac.at/theoret-met/research/raobcore/; NOAA NCDC at www.ncdc.noaa.gov/oa/climate/ratpac/index.php; and the United Kingdom Meteorological Office at <http://hadobs.metoffice.com/hadat/hadat2.html>.

The statements and conclusions in this paper are those of the authors and are not necessarily those of the California Air Resources Board. The mention of commercial products is not to be construed as actual or implied endorsement of such products.

Preface

The California Energy Commission's Public Interest Energy Research (PIER) Program supports public interest energy research and development that will help improve the quality of life in California by bringing environmentally safe, affordable, and reliable energy services and products to the marketplace.

The PIER Program conducts public interest research, development, and demonstration (RD&D) projects to benefit California's electricity and natural gas ratepayers. The PIER Program strives to conduct the most promising public interest energy research by partnering with RD&D entities, including individuals, businesses, utilities, and public or private research institutions.

PIER funding efforts focus on the following RD&D program areas:

- Buildings End-Use Energy Efficiency
- Energy-Related Environmental Research
- Energy Systems Integration
- Environmentally Preferred Advanced Generation
- Industrial/Agricultural/Water End-Use Energy Efficiency
- Renewable Energy Technologies
- Transportation

In 2003, the California Energy Commission's PIER Program established the **California Climate Change Center** to document climate change research relevant to the states. This center is a virtual organization with core research activities at Scripps Institution of Oceanography and the University of California, Berkeley, complemented by efforts at other research institutions. Priority research areas defined in PIER's five-year Climate Change Research Plan are: monitoring, analysis, and modeling of climate; analysis of options to reduce greenhouse gas emissions; assessment of physical impacts and of adaptation strategies; and analysis of the economic consequences of both climate change impacts and the efforts designed to reduce emissions.

The California Climate Change Center Report Series details ongoing center-sponsored research. As interim project results, the information contained in these reports may change; authors should be contacted for the most recent project results. By providing ready access to this timely research, the center seeks to inform the public and expand dissemination of climate change information, thereby leveraging collaborative efforts and increasing the benefits of this research to California's citizens, environment, and economy.

For more information on the PIER Program, please visit the Energy Commission's website www.energy.ca.gov/pier/ or contact the Energy Commission at (916) 654-5164.

Table of Contents

Preface.....	iii
Abstract	xi
1.0 Introduction.....	1
2.0 Data Sources.....	2
2.1. Radiosonde Measurements.....	2
2.2. Surface Temperature Measurements.....	4
2.3. Large-Scale and Regional Model Data	6
3.0 Inversion Characteristics and Measures	6
3.1. Frequency of Strong and Weak Inversions.....	8
3.2. Persistence of Strong and Weak Inversions.....	8
4.0 Results	9
4.1. Inversion Climatology	9
4.1.1. Relationship Between DT_{INV} and $D\theta_{850}$	12
4.1.2. How Representative are the Oakland and San Diego Radiosondes of the Wider Air Basins?	14
4.2. Large-Scale Circulation Patterns Associated with Strong and Weak Inversions...17	
4.2.1. Physical Mechanisms and Inversion Characteristics	22
4.3. Impact of Local Sea Surface Temperature on Inversion Measures	25
4.4. Temporal Variations of Inversion Measures	26
4.4.1. Time Series of Inversion Strength and Inversion Depth	26
4.4.2. Time Series of Strong and Weak Inversion Frequency.....	37
4.4.3. Persistence of Strong and Weak Inversions	39
5.0 Summary and Conclusions	40
6.0 References.....	44
7.0 Glossary	46

List of Figures

- Figure 1. Map of California denoting the radiosonde locations at Oakland, Vandenberg, and San Diego. Also shown on the map are the approximate boundaries of the San Joaquin Valley and South Coast Air Basins. The color contours indicate height above sea level (meters). 4
- Figure 2. Schematic diagram showing some of the measures used to characterize low-level temperature inversions 7
- Figure 3. Monthly mean inversion frequency at Oakland (a, b), Vandenberg (c, d), and San Diego (e, f), determined from twice-daily radiosonde measurements. Subsidence inversion frequency (red curves), radiation inversion frequency (blue curves), and total (subsidence + radiation) inversion frequency (black curves) are shown separately. The data covers the period from 1960–2007. 10
- Figure 4. Box plot diagrams showing the distribution of daily values at 00Z (red) and 12Z (blue) of DT_{INV} , Z_{BASE} , and DZ_{INV} at (a) Oakland, (b) San Diego, and (c) Vandenberg radiosonde locations. Additionally, plots of $D\theta_{850,SJV}$ and $D\theta_{850,SC}$ are included in the Oakland and San Diego columns, respectively. The data covers the period from 1960–2007. 11
- Figure 5. Scatter plots of daily $D\theta_{850}$ vs. DT_{INV} anomalies at Oakland (left column) and San Diego (right column) at 12Z (a, b) and 00Z (c, d). For this comparison, $D\theta_{850}$ was calculated using only radiosonde data. Plots only including days where $Z_{BASE} < 1000$ meters are shown in (e) and (f) for 00Z data. The time period is from 1960–2007. The straight lines represent best linear fits, and the correlation coefficients are shown within each plot. 13
- Figure 6. Plots showing cross-correlation (spatial coherence) of daily mean values of $D\theta_{850}$ from the CaRD10 product relative to locations at (a) Oakland, (b) San Diego, and (c) Vandenberg 16
- Figure 7. Mean geopotential height and vertical velocity at 700 hPa from NCEP Reanalysis product during the 30 days with the largest (a, b) and smallest (c, d) inversion magnitudes ($D\theta_{850,SJV}$ at 12Z) at SJV during the period 1979–2005. The geopotential heights are shown by the color contours and the vertical velocities are denoted by the black contour lines. Contour intervals are 2 pascals per second (Pa sec^{-1}) (JJA [June, July, August]) and 3 Pa sec^{-1} (DJF [December, January, February]), and dashed contours indicate negative (upward) vertical velocity. 17
- Figure 8. Mean geopotential height and vertical velocity at 700 hPa from NCEP reanalysis during the 30 days with the largest (a, b) and smallest (c, d) inversion magnitudes ($D\theta_{850,SC}$ at 12Z) at the South Coast air basin during the period 1979–2005. The geopotential heights are shown by the color contours, and the vertical velocities are denoted by the black contour lines. Contour intervals are 2 Pa sec^{-1} (JJA) and 3 Pa sec^{-1} (DJF) and dashed contours indicate negative (upward) vertical velocity 18

Figure 9. Average values of CaRD10 $D\theta_{850}$ and 10-meter wind during the 30 days with the largest (a, b) and smallest (c, d) observed $D\theta_{850,SJV}$ during time period 1979–2005 for DJF (left column) and JJA (right column). The white line denotes the approximate boundary of the San Joaquin Air Basin. The color filled contours indicate the CaRD10 $D\theta_{850}$ values; the vector arrows represent the 10-meter winds..... 20

Figure 10. Average values of CaRD10 $D\theta_{850}$ and 10-meter wind during the 30 days with the largest (a, b) and smallest (c, d) observed $D\theta_{850,SC}$ during time period 1979–2005 for DJF (left column) and JJA (right column). The white line denotes the approximate boundary of the South Coast Air Basin. The color filled contours indicate the CaRD10 $D\theta_{850}$ values while the vector arrows represent the 10-meter winds..... 21

Figure 11. Time series of filtered monthly mean values of (a) 12Z DT_{INV} , (b) 00Z DT_{INV} , (c) 12Z $D\theta_{850,SJV}$, (d) 00Z $D\theta_{850,SJV}$, (e) 12Z DZ_{INV} , (f) 00Z DZ_{INV} , (g) 12Z Z_{TOP} and Z_{BASE} , and (h) 00Z Z_{TOP} and Z_{BASE} based on the Oakland radiosonde data and surface temperature measurements in the San Joaquin Valley air basin. For each variable a six-month running mean (green line) and a five-year running mean filter (red line) are shown except for the bottom row of plots showing Z_{TOP} and Z_{BASE} , where only the five-year running mean filtered data is shown for clarity. The straight blue lines represent a linear best fit to the data. The monthly means were calculated using only days when subsidence inversions were observed..... 27

Figure 12. Time series of filtered monthly mean values of (a) 12Z DT_{INV} , (b) 00Z DT_{INV} , (c) 12Z $D\theta_{850,SC}$, (d) 00Z $D\theta_{850,SC}$, (e) 12Z DZ_{INV} , (f) 00Z DZ_{INV} , (g) 12Z Z_{TOP} and Z_{BASE} , and (h) 00Z Z_{TOP} and Z_{BASE} based on the San Diego radiosonde data and surface temperature measurements in the South Coast air basin. For each variable a six-month running mean (green line) and a five-year running mean filter (red line) are shown, except for the bottom row of plots showing Z_{TOP} and Z_{BASE} where only the five-year running mean filtered data is shown for clarity. The straight blue lines represent a linear best fit to the data. The monthly means were calculated using only days when subsidence inversions were observed. Note: Data gaps in some of the filtered data curves are due to some months with no subsidence inversions. 28

Figure 13. Time series of annual mean values of DT_{INV} (a, b), $D\theta_{850}$ (c, d), DZ_{INV} (e, f), based on radiosonde data and surface temperature measurements in the San Joaquin Valley ($D\theta_{850,SJV}$) and South Coast ($D\theta_{850,SC}$) air basins. The green line shows the annual mean data, while the red line show a five-year running mean. The straight blue lines represent a linear best fit to the data. The annual means were calculated using only days when radiation inversions were observed at 12Z..... 37

Figure 14. Time series of monthly frequency of strong and weak inversions at Oakland (a, c) and San Diego (b, d). Red curves show the frequency of strong inversions while the blue curve shows the frequency of weak inversions. The data was smoothed using a six-month running mean (thin lines) and five-year running mean (thick curves) filters. The straight lines represent a linear best fit. Strong inversions are defined when DT_{INV} exceeds the third

quartile and weak inversions are defined when DT_{INV} is less than the first quartile value. Quartiles were calculated for each calendar month using detrended daily values of DT_{INV} derived from radiosonde measurements over the 1960–2007 period at each site. 38

List of Tables

Table 1. Maximum/Minimum inter-station θ_{2M} correlations for both daily values and monthly means. Surface temperatures are from available cooperative observer stations within Southern California and the San Joaquin Valley.	14
Table 2. Correlations of T_{850} between radiosonde locations for both daily values and monthly means. No overlap (NO) indicates there were less than 30 days in common between a particular station pair.	15
Table 3. Correlations between monthly mean values of local SST and various inversion measures at Oakland and San Diego. Correlations greater than 0.19 at San Diego and 0.22 at Oakland are significant at the 95% confidence level.	26
Table 4. Correlation between 1960–2007 filtered monthly means: Inversion measures vs. SST indices. Monthly means of the inversion measures are for subsidence inversions only. The time series were detrended and then filtered using a 12-month running mean. Correlations greater than 0.28 are significant at the 95% confidence level.	29
Table 5. Change in magnitude of several inversion measures during the period 1960–2007 calculated from radiosonde measurements. Results are for subsidence-type inversions. The values shown in parentheses are the absolute changes in magnitude normalized by the standard deviation of the annual means for each variable, location, and launch time. Note: $D\theta_{850}$ values were calculated using radiosonde data and surface temperature observations in the San Joaquin Valley and South Coast air basins.	30
Table 6. Correlation of daily values from 1960–2007 Oakland 00Z radiosonde measurements. The correlations were calculated using only days when a subsidence inversion was observed in the radiosonde data. The various time series were detrended prior to calculation.	33
Table 7. Correlation of monthly means from 1960–2007 Oakland 00Z radiosonde measurements. The monthly means were calculated using only those days when a subsidence inversion was observed in the radiosonde data. The various time series were detrended prior to calculation.	33
Table 8. Correlation of daily values from 1960–2007 San Diego 00Z radiosonde measurements. The correlations were calculated using only days when a subsidence inversion was	

observed in the radiosonde data. The various time series were detrended prior to calculation.	34
Table 9. Correlation of monthly means from 1960–2007 San Diego 00Z radiosonde measurements. The monthly means were calculated using only those days when a subsidence inversion was observed in the radiosonde data. The various time series were detrended prior to calculation.....	34
Table 10. Correlation of low-frequency subsidence inversion variability (five-year running mean filter) from 1960–2007 Oakland 00Z radiosonde measurements. The various time series were detrended prior to calculation.	35
Table 11. Correlation of low-frequency subsidence inversion variability (five-year running mean filter) from 1960–2007 San Diego 00Z radiosonde measurements. The various time series were detrended prior to calculation.	36
Table 12. Average number of strong inversion days per year based on time series of DT_{INV} that was not detrended. Values are given for the first and second half of the period.	39
Table 13. Average value of persistence parameter PV.....	40

Abstract

This research examined the variability of low-level inversions in California, using historical observations from about 1960 through 2007. The emphasis was on the two air basins of primary concern in California: the South Coast and San Joaquin Valley. A range of time scales were investigated, from synoptic events of just a few days to low-frequency decadal fluctuations and trends over the entire period of record. Inversions are a common feature throughout California, present more than 65 percent of winter days and nearly 100 percent of summer days. When the strength of the inversion is defined as a difference of temperature between the top and the bottom of the inversion layer, strong inversions tend to be thicker, and weak inversions tend to be thinner in their vertical extent. There is a strong connection between large-scale circulation features and inversion events, with strong inversions associated with high pressure systems over California and weak inversions associated with low pressure systems. Physical processes associated with these circulation features (including horizontal and vertical temperature advection), as well as the interaction of these processes, are shown to affect inversion structure and variability. Strong and weak inversions tend to cluster into multi-day episodes, as driven by synoptic-scale weather and perhaps other lower-frequency climate patterns. Inversion frequency varies on interannual to decadal time scales, partly in association with sea surface temperature anomalies along the California coast. Accordingly, there is an association between inversion strength and El Niño/Southern Oscillation events and also, perhaps stronger than the El Niño/Southern Oscillation, association to the Pacific Decadal Oscillation. Radiosonde measurements show significant trends in many inversion measures over the 1960–2007 study period. Specifically, inversion strength decreased and inversion layer thickness decreased at sites in California. Accompanying changes toward higher and warmer inversion base and lower and somewhat warmer inversion tops have also occurred. These trends are in part due to changes in processes associated with large-scale atmospheric circulation changes, but local surface influences may also play a role.

Keywords: Temperature inversions, California climate, air quality, climate variability, radiosonde

1.0 Introduction

Concentration of key air pollutants (e.g., ozone and secondary particulate matter) depends strongly upon the vertical gradient of temperature (e.g., inversion strength) in the lower atmosphere. California's setting, featuring strong subsidence along the flank of the North Pacific High and the containment within coastal and interior valleys, produces regularly occurring low-level inversions and thus chronic air quality problems. Low-level atmospheric temperature inversions (where temperature increases with height) inhibit vertical movement of air and can thereby increase the concentrations of pollutants near the ground. As the climate and regional circulation patterns change, the frequency and intensity of low-level temperature inversions will be affected in an unknown manner. A variation in the frequency or intensity of these low-level inversions would likely have a significant impact on air quality in California.

There are two basic types of low-level inversions: radiation (or surface) inversions and subsidence inversions. *Radiation (or surface) inversions* typically occur at night when there is no incoming solar radiation to balance the surface cooling due to outgoing longwave radiation. These inversions are usually at their maximum strength around sunrise, but often survive well into the daylight hours. Valley regions are especially prone to radiation inversions due to cold air drainage along the slopes of the valley margins. In the San Joaquin Valley, concentrations of particulate matter, which are generally at a maximum during the winter season, are affected by the interaction of a relatively shallow radiation inversion layer and a higher valley wide inversion layer (Watson and Chow 2002).

Subsidence inversions occur due to higher level, broad-scale sinking motions associated with high pressure systems along with lower level turbulence within the surface mixed layer (Tennekes 1973). The combination of these processes produces an inversion layer that is lifted away from the surface even during the early morning hours, whereas the base of a radiation inversion is at the surface. The relatively cool moist air in the marine boundary layer typical of the Southern California coastal region can intensify and prolong subsidence inversions. Effects of sea breezes and mountain-valley topography can also be important factors in the evolution of the inversion layer and associated pollution events (Lu and Turco 1994; Wakimoto 1987). The San Joaquin Valley is also subject to subsidence inversions during summer, with ozone pollution levels near that of the Los Angeles region. In the San Joaquin Valley local wind orientation plays a key role, as most of the pollutants are transported from remote source regions (Dabdub et al. 1999).

Previous studies have examined the effect of climate on regional air quality in the central and eastern portions of the United States (Hogrefe et al. 2004; Mickley et al. 2004). These studies used output from Global Climate Models (GCMs) to study the frequency of large-scale weather patterns that promote the formation of air pollution events. The results of these previous studies predict that the frequency of summer ozone air pollution events in the central and eastern United States will increase in the future due to altered climate and increased background concentrations of ozone. The GCM output can also be dynamically downscaled using regional meteorological models to simulate air pollution formation with regional air quality models. Steiner et al (2006) used this approach to examine the effects of regional climate change and future emission scenarios on ozone formation in central California. Their results indicate that

changes in meteorological variables associated with future climate changes would increase daily peak ozone concentrations in central California. Along similar lines, a recent study assessing effects of temperature on ozone concentrations in California's South Coast and San Joaquin air basins by Mahmud et al. 2008 indicates that projected future warming would produce significant increases in the occurrence of days with hazardous ozone concentrations.

California has warmed over the last few decades, with temperature increases exceeding levels that would likely be expected solely from natural climate variability (Bonfils et al. 2008). Virtually all climate model projections indicate that California's climate will warm as greenhouse gases continue to accumulate in the atmosphere (Cayan et al. 2008). Based upon recent runs over a variety of models and greenhouse gas emissions scenarios, potential warming over California during the twenty-first century would range from about 2°C to 5°C, or 3.6°F to 9°F (change of temperatures in 2100 relative to recent 1961–1990 historical climatology) (Cayan et al. 2008). This degree of warming over California would be associated with significant changes in circulation and other facets of the climate over the region, as indicated by results from regional modeling studies (e.g., Snyder et al. 2002; Duffy et al. 2006). Because the magnitude of these changes may rival or exceed the magnitude of natural year-to-year climate variability in California, these changes could have significant consequences on the production and buildup of air pollutants in California's air basins. To build an understanding of how these factors may change, it seems important to examine the available record of historical variability of low-level inversions.

The focus of this paper is to investigate the occurrence, variability, and regional to large-scale causal factors of low-level inversions in California. Historical observations from about 1960 through 2007 are examined. The emphasis is on the two air basins of primary concern in California: the South Coast and San Joaquin air basins that are generally subjected to the highest air pollution levels in the state. The historical data is used to determine the climatological strength and frequency of inversion at different sites in California. Large-scale circulation patterns and meteorological variables associated with strong and weak inversions are also investigated. The influence of interannual to decadal climate modes on the frequency and persistence of strong inversions is examined and discussed. Finally, temporal trends in various inversion measures over the historical period are calculated and evaluated.

In Section 2 we outline the various data sets utilized in this study. The different measures used to quantify and characterize inversions are discussed in Section 3. In Section 4 we present the results of various analyses.

2.0 Data Sources

2.1. Radiosonde Measurements

Radiosonde measurements provide a detailed vertical profile of temperature, pressure, dew point, and horizontal winds, and are well suited to study low-level temperature inversions. Radiosonde data over the United States is collected and archived by Earth System Research Laboratory (ESRL) of the National Oceanic and Atmospheric Administration (NOAA) (Schwartz et al. 1992). Routine radiosonde profiles are made twice daily at 0Z and 12Z at

locations within the United States, including three sites in California: at San Diego, Vandenberg, and Oakland. These observations date from 1960 to present (some data exists prior to 1960 but is not used in this study due to uncertainties and irregular launch times). In addition to the three primary sites, parts of this study also included some less-continuously sampled radiosonde observations from Long Beach, Santa Monica, and Merced. Figure 1 shows the location of the California radiosonde sites and the proximity to the main air basins of interest in this study.

The site of the San Diego radiosonde observation moved in 1989 from Montgomery Field to Miramar Naval Air Station. The distance between the old and new sites is about 6 kilometers (km), and the difference in elevation is only 23 meters (m). Both Montgomery Field and Miramar Naval Air Station are approximately the same distance (12 km) from the Pacific Ocean. It is expected that the impact of the site move would be minimal on measured upper air temperatures due to the similar geography and proximity to the Pacific Ocean. However, the impact on the surface temperature may be more significant, as even slight changes in the local conditions at and near the surface could have an appreciable effect.

Radiosonde instrumentation and processing algorithms have undergone changes over the time period examined in this paper. These changes appear to have led to differences in the vertical resolution of temperature readings between the surface and the 700 hectopascal (hPa) level at both Oakland and San Diego. At both sites there was a gradual increase in average number of temperature readings (surface to 700 hPa) from about 10 in 1960 to about 14 in the late 1980s. After this time, the number increased to about 20 in 1990 and then dropped dramatically to about 10–11 in 1998. Some of these changes in vertical resolution can be traced to the addition or removal of standard reporting levels. However, causes of other changes in vertical resolution are not so easily identified.

To address this variability in vertical resolution, the radiosonde records were resampled to produce a data set with a consistent vertical resolution throughout the time period 1960–2007. The vertical resolution of this resampled data set was 10 temperature readings equally spaced (pressure-wise) between the 1000 and 700 hPa levels. Tests were conducted on this “coarsened” data set to examine the possible sensitivity of our results to the changing vertical resolution. Analyses of the coarsened data yielded similar trends as those obtained using the original radiosonde records.

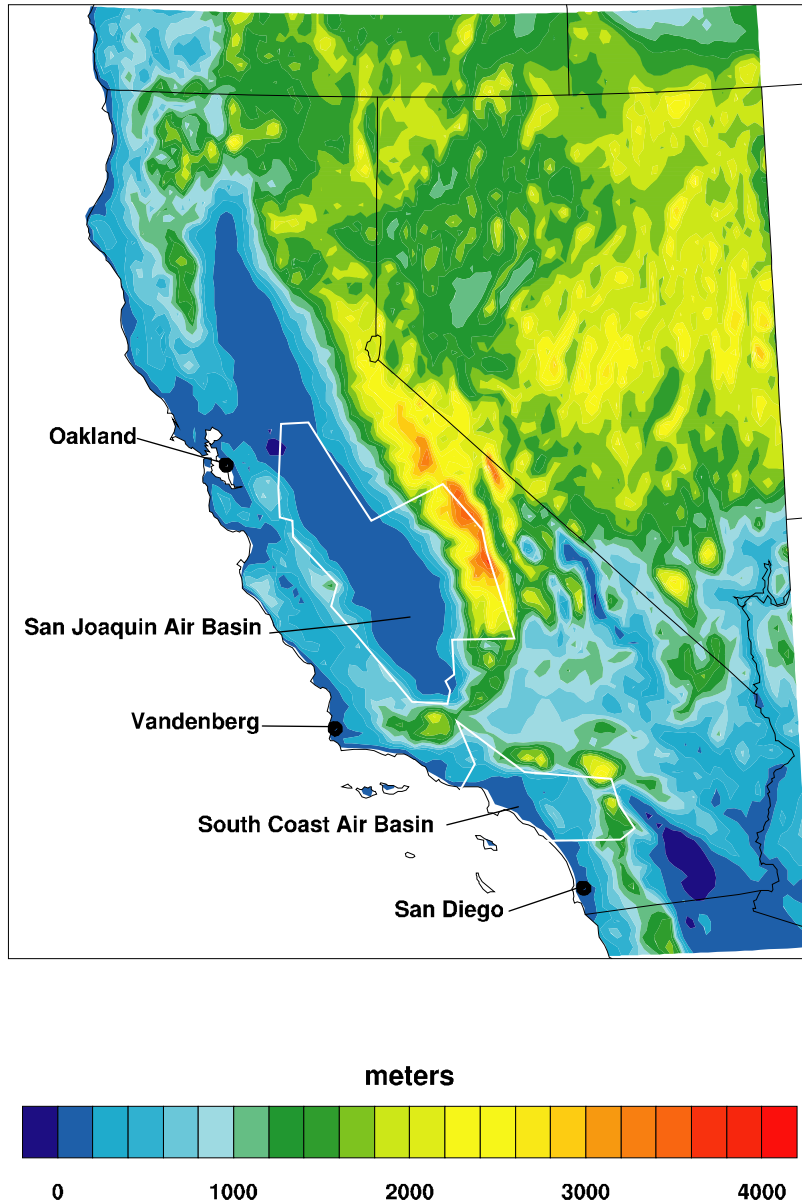


Figure 1. Map of California denoting the radiosonde locations at Oakland, Vandenberg, and San Diego. Also shown on the map are the approximate boundaries of the San Joaquin Valley and South Coast Air Basins. The color contours indicate height above sea level (meters).

2.2. Surface Temperature Measurements

Surface measurements from the soundings in San Diego and Oakland were not used in the analysis of long-term variability because they are generally not representative of surface temperature conditions in the South Coast Basin and San Joaquin Valley. Additionally, the sounding record in San Diego suffers from inhomogeneities due to several site changes. Unfortunately, there are no single-site records of hourly temperature observations that extend

over the entire time period. The only homogeneous long-term daily surface temperature measurements available are maximum (Tmax), minimum (Tmin), and mean temperature from the Global Historical Climatology Network (Version 2) (GHCN2) (Peterson and Vose 1997). The GHCN2 data in California come from NOAA's Cooperative Observing stations that experienced very few and very small changes in location over time. Peterson and Vose (1997) describe statistical methods that were used to detect and correct inhomogeneities in the monthly mean GHCN2 station time series. They adjusted the station time series by adding or subtracting a correction factor for each month. Unlike the case for monthly mean values, daily values of Tmax and Tmin in the GHCN2 did not include any adjustments for inhomogeneities. We therefore added or subtracted the GHCN2 monthly correction factor for all days in the respective month. After doing so, the daily GHCN2 Tmax and Tmin station time series no longer had inhomogeneities (to the extent that the monthly correction factors were reliable). A few stations that experienced large or highly variable adjustments were discarded. Long-term trends for adjusted and non-adjusted time series exhibited little difference.

Since daily maximum temperature typically occurs in the afternoon and daily minimum temperature typically occurs shortly before sunrise, Tmax in Pacific Time generally occurs close in time to 00Z and Tmin in Pacific Time generally occurs close in time to 12Z. A difference between surface observing time and sounding observing on the order of a couple hours should not matter much, since the diurnal cycle in temperature above the boundary layer is small. For the purposes of our study, it may be in fact be beneficial that the time of surface maximum temperature generally corresponds to the time of day when the boundary layer is least stable and the time of surface minimum temperature generally corresponds to the time of day when the boundary layer is most stable.

The nominal observing procedure is that the maximum and minimum temperatures occurring in the 24-hour period prior to the time of observation are reported as Tmax and Tmin. Observing times range from 6 local time (LT) to 18 LT. Irrespective of observing time, Tmin will almost always correspond to the minimum during the previous night. That is not the case for Tmax, which could correspond to the maximum temperature during the previous local day for a morning observing time or the maximum temperature during the same local day for a late afternoon observing time. Unfortunately, information on observing time is uncertain, and it moreover appears that some stations reported Tmax as maximum temperature that occurred several hours after a nominal morning observing time. To find the appropriate coordinated universal time (UTC) day on which to assign a Tmax measurement, correlations at various lead/lags were calculated between Tmax and 00Z National Centers for Environmental Prediction (NCEP) Reanalysis 995 sigma level temperature (T995) interpolated to the station location. These correlations were calculated for each month, and the results indicated that there were multi-year blocks of time where Tmax had best correspondence with 00Z T995 from the same UTC day (previous local day) and other blocks of time where Tmax had best correspondence with 00Z T995 from the following UTC day (same local day). Errors in the assignment of Tmax day should have minimal impact on the results since the decorrelation time for Tmax is on the order of 7–13 days.

For purposes of better comparability, temperature was converted to potential temperature using values of 00Z and 12Z NCEP Reanalysis sea level pressure interpolated to the station location.

Regional average maximum and minimum potential temperature time series were created by separately averaging station climatologies and station anomalies. This will minimize geographical biases when one station has missing data (spatial gradients in temperature anomalies are smaller than gradients in climatological temperature). Daily station anomalies were calculated from a climatology made from the first five harmonics fit to the annual cycle. A regional time series was created for the South Coast air basin using stations at Chula Vista, Irvine Ranch, Pasadena, and Redlands, while a time series representative of the San Joaquin Valley was constructed with station data from Wasco, Lemon Cove, Hanford, Fresno, Merced, and Lodi.

2.3. Large-Scale and Regional Model Data

Data from the NCEP Reanalysis 1 product (Kalnay et al. 1996) is used in this study to provide insight into the large-scale circulation patterns that are associated with the strength and frequency of inversions in California. The NCEP Reanalysis project assimilates available past observational data into a state-of-the-art atmospheric model to produce dynamically consistent data on a global grid with a horizontal resolution of 2.5 degrees and 17 vertical pressure levels. The data has a temporal coverage of 1948 to present at a six-hour resolution.

While the NCEP reanalysis products are sufficient to produce large-scale circulation patterns, the horizontal and temporal resolution is too coarse to provide enough detail over the highly variable surface topography of California. In the present study, data from the California Reanalysis Downscaling at 10 km (CaRD10) is used to estimate local to regional-scale weather patterns over and within California air basins. Data from NCEP Reanalysis 1 for the period 1948–2005 was dynamically downscaled to 10-km resolution using the Regional Spectral Model (RSM) (Kanamitsu and Kanamaru 2007; Kanamaru and Kanamitsu 2007). Validation of the downscaled products found that near-surface wind and temperature fit better to regional-scale station observations than the large-scale reanalysis used to force the regional model as well as the regional data assimilation North American Regional Reanalysis (Mesinger et al. 2006) (Kanamaru and Kanamitsu 2007). The near-surface data and free atmospheric data on 17 vertical pressure levels are available. The data have a temporal coverage of 1948 to 2005 at hourly resolution.

3.0 Inversion Characteristics and Measures

A schematic illustration of a typical inversion temperature profile is shown in Figure 2. To quantify an inversion, several different measures are used, including the height of the base (Z_{BASE}) of the inversion, the height of the top (Z_{TOP}) of the inversion, the temperature at the base (T_{BASE}) of the inversion, the temperature at the top (T_{TOP}) of the inversion, the temperature difference across the inversion (DT_{INV}), the depth of the inversion (DZ_{INV}) and the temperature lapse rate within the inversion. Accurate computation of these quantities generally requires high-resolution vertical profiles of temperature. The potential temperature difference ($D\theta_{850}$)

between 850 hectopascals (hPa) and the surface (2 meters) as well as θ_{850} alone have also been used (Ferreria and Shipp 2005) as measures of inversion strength. This paper uses both DT_{INV} and $D\theta_{850}$ to measure the strength of the inversion, where a larger positive value indicates a stronger inversion.

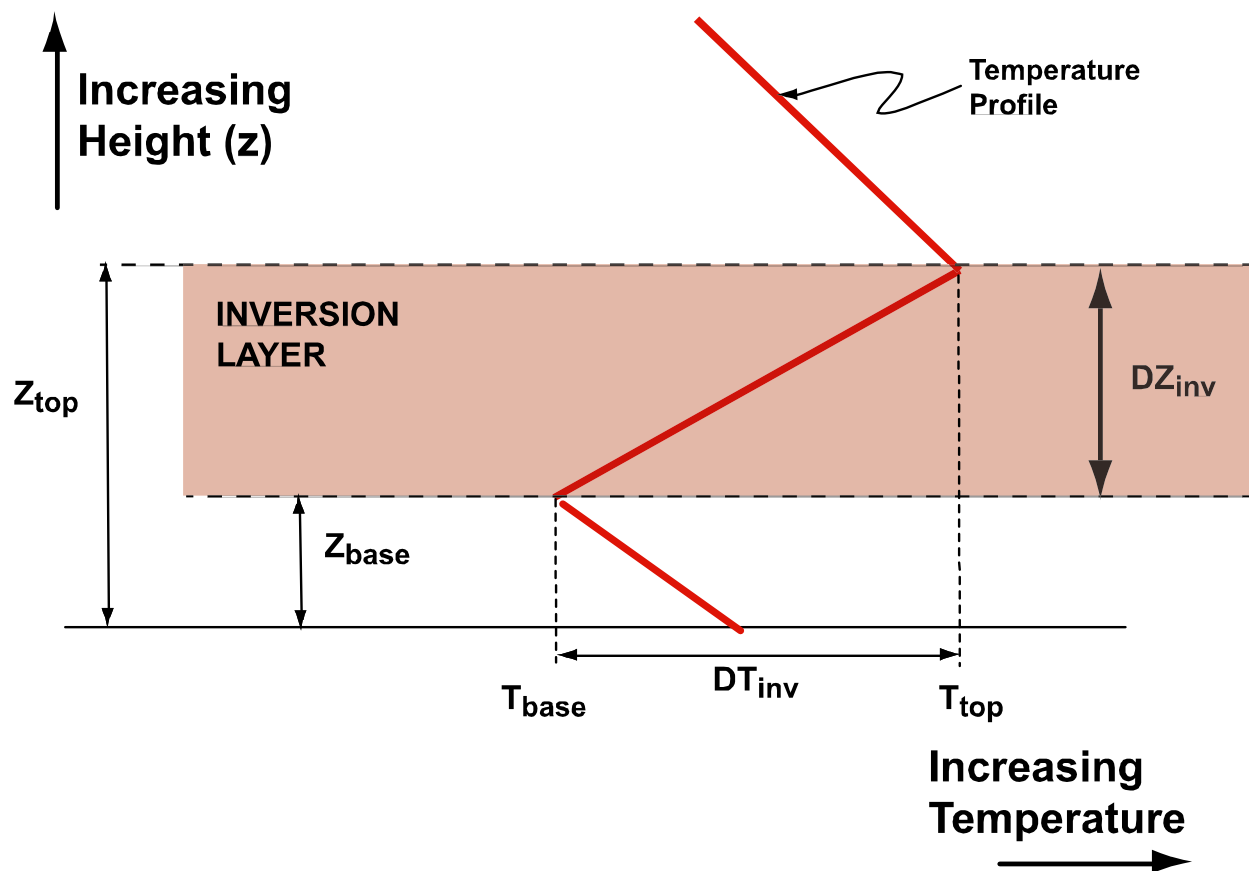


Figure 2. Schematic diagram showing some of the measures used to characterize low-level temperature inversions

Although DT_{INV} has the advantage of being a direct measurement of inversion strength, it can only be obtained at the few sites where sounding observations are present. One would expect that temperatures within the boundary layer, in particular the inversion base temperature, to depend on surface characteristics that are highly variable throughout California. As a result, DT_{INV} may not be entirely representative of conditions away from the measurement region.

While not a direct measure of a temperature inversion, $D\theta_{850}$ can be estimated at a larger number of locations than DT_{INV} . The relatively large spatial coherence of temperatures above the boundary layer allows using radiosonde values of θ_{850} along with abundant ground-based surface temperature observations to estimate $D\theta_{850}$. For example, this paper will often use θ_{850} from San Diego radiosonde measurements together with surface temperature observations in the South Coast air basin to estimate a $D\theta_{850}$ applicable to this air basin. These values will be

denoted as $D\theta_{850,SJV}$ and $D\theta_{850,SC}$ depending on where the surface temperature observations were obtained, either the San Joaquin Valley and South Coast air basins, respectively. Another advantage of using $D\theta_{850}$ is that this quantity is easily obtained from the standard output of most climate models. In Section 4 we examine the spatial and temporal relationships between DT_{INV} and $D\theta_{850}$.

Additionally, the stability of the mid-to-lower atmosphere above the inversion layer, while not a direct measure of inversion strength, is used to help understand and interpret inversion characteristics and variability. Here the potential temperature lapse rate between 850 and 500 hPa ($d\theta/dz_{850-500}$) is used to measure the mid-to-lower atmospheric stability.

Some important conventions were adopted in calculating DT_{INV} , DZ_{INV} , and Z_{BASE} . First, the temperature profile, between the surface and 700 hPa level, is examined for temperature inversions, defined to be present when a temperature at a given altitude in the sounding was warmer than the temperature at an altitude below it. In the case when more than one inversion is observed, the largest inversion in terms of DT_{INV} is used. Subsidence inversions were defined as having a base level at least 50 meters above the surface. Radiation inversions are defined as cases when the base of the temperature inversion lies at the surface. In most cases, subsidence inversions are examined separately from radiation inversions in this study.

3.1. Frequency of Strong and Weak Inversions

Daily anomaly values of DT_{INV} from the set of all inversions (subsidence and radiation inversions together) were used to estimate the frequency of strong and weak inversions. To compute the strong inversion frequency, the 1960–2007 radiosonde DT_{INV} time series was detrended to remove any long-term trends that might bias the results. Climatological monthly values of DT_{INV} were calculated from the 48 years of data. Climatological daily values were obtained by linearly interpolating between the climatological monthly values.

The daily anomaly values for each calendar month (approximately $48 \times 30 = 1440$ values) were sorted and the quartile points calculated. A day was considered to have a “strong inversion” if its daily DT_{INV} anomaly value exceeded the third quartile (Q_3) level; similarly a day was identified as having a “weak inversion” if its daily DT_{INV} anomaly value was less than the first quartile (Q_1). Thus, over the entire time series, 25% of the days would be labeled as having a strong inversion and 25% of days were labeled as a weak inversion. Of course, individual months may have a strong or weak inversion frequency of more or less than 25%.

3.2. Persistence of Strong and Weak Inversions

Persistence of different categories of strength of inversion was measured using the detrended DT_{INV} time series and quartile points described above. A persistence value (PV) was calculated for each day, where:

$$PV(i) = 0 \text{ if } DT_{INV} < Q_3 \text{ for day } i$$

$$PV(i) = N \text{ if } DT_{INV} > Q_3 \text{ for day } i, \text{ where } N \text{ is the number of contiguous previous days (including present day) where } DT_{INV} > Q_3.$$

For example, a value of $PV(i)=3$ would indicate that $DT_{INV} > Q_3$ for the present day i as well as the two previous days $i-1$ and $i-2$ and $DT_{INV} < Q_3$ on day $i-3$. Larger values of PV indicate persistence (or episodes) of continuously strong inversion days. The example above defines the persistence of inversions in the fourth (highest strength) quartile, but will also be applied easily to the other three quartiles.

4.0 Results

4.1. Inversion Climatology

The seasonal cycle of monthly mean subsidence and radiation inversion frequency at Oakland, Vandenberg, and San Diego is shown in Figure 3 for both the 00Z (local 4 p.m. Pacific Standard Time, PST) and 12Z (local 4 a.m. PST) soundings. The data shown in the plots were derived from daily radiosonde measurements at these sites during the period 1960–2007. At all locations summer months are dominated by subsidence inversions. During winter, radiation inversions are more frequent in the early morning at 12Z and nearly absent in mid afternoon at 00Z. At 12Z (4 a.m. local time) radiational cooling of the surface has just about reached a maximum, allowing radiation inversions to more easily form, while at 00Z (4 p.m. local time) solar heating has warmed the surface sufficiently to eliminate nearly all radiation inversions. For the early morning 12Z reading, the annual mean frequency of radiation inversions at Oakland, Vandenberg, and San Diego is about 32%, 43%, and 39%, respectively. This agrees reasonably well with Neiburger (1969) who estimates that radiation inversions are present in California about 40% of the time.

Perhaps the most striking detail in Figure 3 is the high frequency of inversion occurrence (either subsidence or radiation) at all three locations throughout the year. During summer months, inversions of various magnitudes are almost always present at these sites, while during winter months low-level temperature inversions are present at least 65% of the time. Even when no inversion was present, the lower atmosphere was often quite stable. For example, 75% of the non-inversion days (00Z sounding) had regions below the 700 hPa level at least 50 hPa thick with values of $d\theta/dz > 3.2$ degrees Kelvin per kilometer ($K\ km^{-1}$) at San Diego and $d\theta/dz > 3.4\ K\ km^{-1}$ at Oakland.

The magnitude and variability of daily values of four measures for subsidence inversions are shown in Figure 4 as a function of calendar month. Data is only included for those instances when a subsidence inversion was present. Data is shown for $D\theta_{850,SJV}$ (or $D\theta_{850,SC}$), DT_{INV} , Z_{BASE} , and DZ_{INV} at both 00Z and 12Z radiosonde launch times. Recall, the $D\theta_{850,SJV}$ and $D\theta_{850,SC}$ measures use radiosonde 850 hPa temperature and mean surface temperature from the selected stations within the appropriate air basin, San Joaquin Valley (SJV) or South Coast (SC).

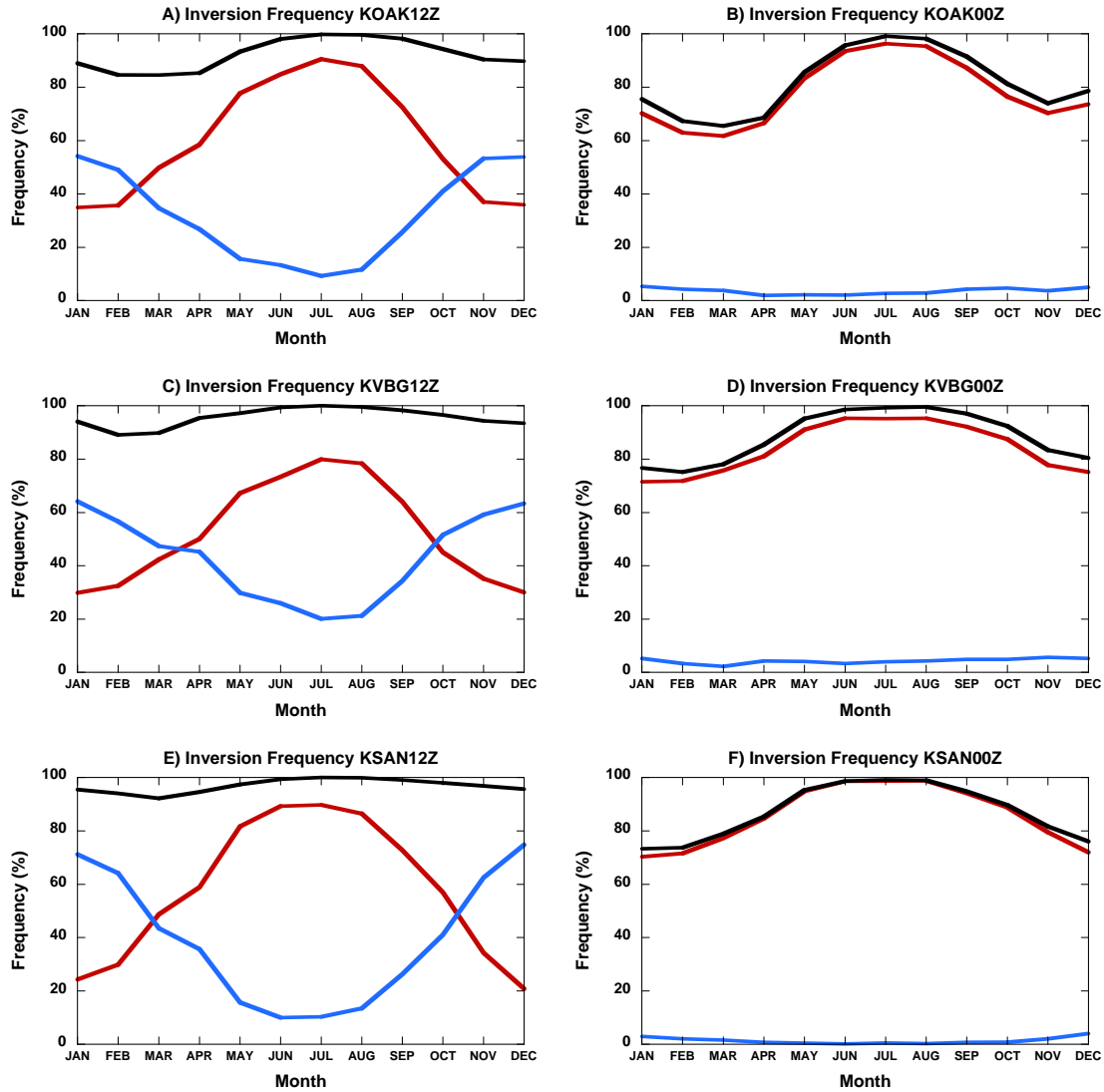


Figure 3. Monthly mean inversion frequency at Oakland (a, b), Vandenberg (c, d), and San Diego (e, f), determined from twice-daily radiosonde measurements. Subsidence inversion frequency (red curves), radiation inversion frequency (blue curves), and total (subsidence + radiation) inversion frequency (black curves) are shown separately. The data covers the period from 1960–2007.

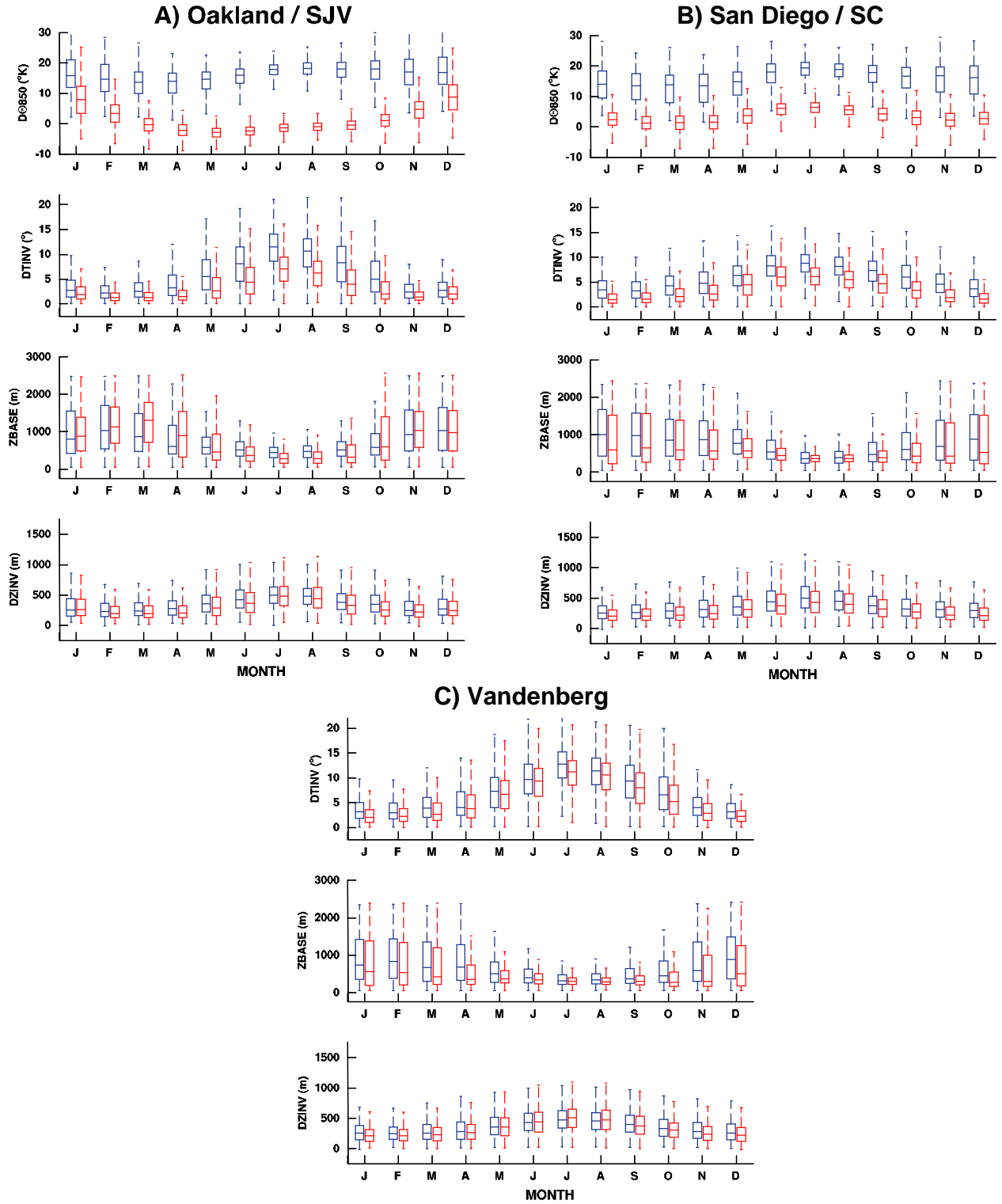


Figure 4. Box plot diagrams showing the distribution of daily values at 00Z (red) and 12Z (blue) of DT_{INV} , Z_{BASE} , and DZ_{INV} at (a) Oakland, (b) San Diego, and (c) Vandenberg radiosonde locations. Additionally, plots of $D\theta_{850,SJV}$ and $D\theta_{850,SC}$ are included in the Oakland and San Diego columns, respectively. The data covers the period from 1960–2007.

Throughout the year, the magnitude of both DT_{INV} and $D\theta_{850}$ is larger at 12Z compared to 00Z. However, the seasonal variability, especially at 00Z and especially at Oakland is very different for $D\theta_{850}$ as compared to DT_{INV} . The magnitude and variability of DT_{INV} at 00Z and 12Z increase during summer at all locations. In contrast, $D\theta_{850}$ variability is at a minimum during summer, while the magnitude does not show much change over the course of the year except for the Oakland/SJV 00Z, when the $D\theta_{850}$ magnitude decreases significantly. Daily values of inversion top temperature and θ_{850} had correlations greater than 0.9 at both Oakland and San Diego, while correlations between the temperature at a height of two meters (T_{2m}) and inversion base temperature were lower, at 0.6–0.8, although still highly significant. This indicates that the differences in seasonal and diurnal behavior between $D\theta_{850}$ and DT_{INV} are most likely due to using regional mean surface temperatures to represent T_{2M} in the computation of $D\theta_{850}$.

The inversion base height (Z_{BASE}) is lower during summer than winter and also has lower variability during the summer months than winter months—this is the case at all three locations and at the 12Z and 00Z radiosonde launch times. Compared to Z_{BASE} , the seasonal differences in inversion depth (DZ_{INV}) are significantly smaller, with only a slight increase in both magnitude and variability during summer.

4.1.1. Relationship Between DT_{INV} and $D\theta_{850}$

To examine how well the $D\theta_{850}$ measure represents DT_{INV} , daily anomaly values determined from radiosonde measurements are compared in Figure 5. For these comparisons, $D\theta_{850}$ values were computed using surface temperature from the radiosonde measurement, so that both DT_{INV} and $D\theta_{850}$ are representative of the same location. There is a moderate-to-strong correspondence between DT_{INV} and $D\theta_{850}$ anomalies at both Oakland and San Diego, with correlations greater than 0.60 (Figure 5a–d).

Higher correlations, approximately 0.7–0.8, are noted at the 12Z time, probably reflecting the less complicated structure in the morning and subsequent lifting of the inversion layer higher away from the surface as the afternoon progresses. This upward movement of the inversion layer is due to increased surface heating and to increasing entrainment free atmospheric air above the inversion layer. As the inversion layer moves upward it can begin to impact the temperature at 850 hPa. The linear fit shown in Figures 5c–5d does not well represent the distribution and appears to be due to including inversions with vastly different base heights. When days when $Z_{BASE} > 1000\text{m}$ are eliminated from the 00Z comparison (Figure 5e–5f), the correlations between DT_{INV} and $D\theta_{850}$ improves markedly and are similar to 12Z values.

While certainly not conclusive, these results suggest that $D\theta_{850}$ is generally a reasonable indication of the actual inversion strength DT_{INV} . However, it should be noted that the above comparisons were performed at only two sites, both of which are coastal locations.

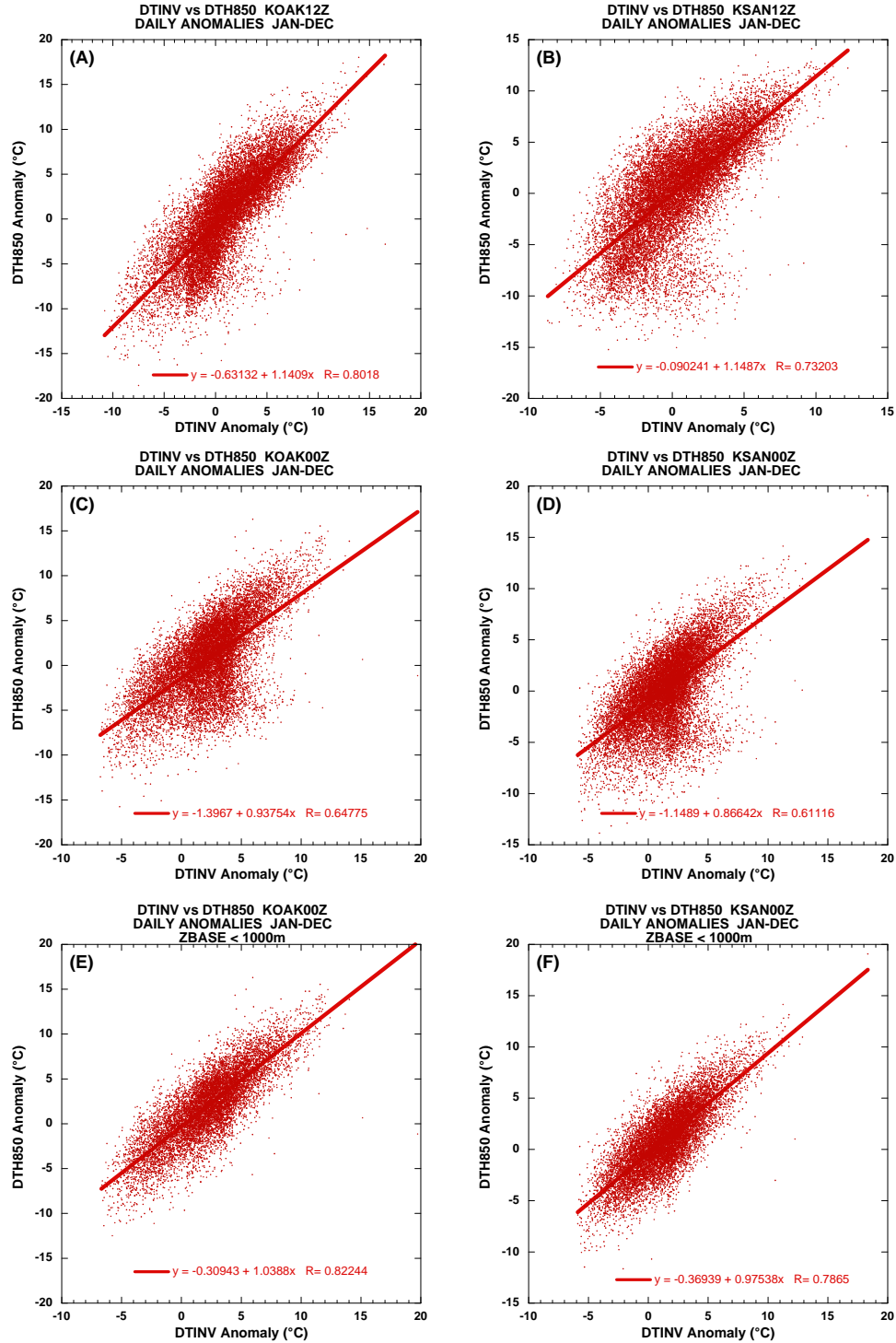


Figure 5. Scatter plots of daily $D\theta_{850}$ vs. DT_{INV} anomalies at Oakland (left column) and San Diego (right column) at 12Z (a, b) and 00Z (c, d). For this comparison, $D\theta_{850}$ was calculated using only radiosonde data. Plots only including days where $Z_{BASE} < 1000$ meters are shown in (e) and (f) for 00Z data. The time period is from 1960–2007. The straight lines represent best linear fits, and the correlation coefficients are shown within each plot.

4.1.2. How Representative are the Oakland and San Diego Radiosondes of the Wider Air Basins?

Historical sounding records in California are restricted mostly to coastal or near-coastal sites in Oakland, San Diego, and to lesser extent, at Vandenberg Air Force Base. Are the thermal structure and inversion characteristics at just a few locations a reasonable representation of the key air basins in the state? To this end, it has been noted above that the diurnal and seasonal nature of the frequency and strength of subsidence inversions and of radiation inversions is quite similar across the three sounding locations. The anomalous variability, on daily and monthly time scales, is well correlated across several locations (see Tables 1 and 2). Surface temperatures, taken from available cooperative observer stations in Southern California and from the San Joaquin Valley, are well correlated, as demonstrated in Table 1. For Southern California, the weakest inter-station daily anomaly correlation is 0.54 (summer Tmax for Chula Vista-Redlands) and the strongest correlation is 0.89 (winter Tmax for Pasadena-Redlands). For the San Joaquin Valley, the weakest daily correlation is 0.64 (summer Tmin for Hanford-Lodi) and the strongest is 0.94 (summer Tmax for Fresno-Lemon Cove). Longer time scale surface temperature variations, formed from monthly and annual mean anomalies, are also generally well correlated, with correlations ranging from 0.49–0.91 (monthly) and 0.34–0.89 (annual) for Southern California and 0.36–0.94 (monthly) and 0.56–0.86 (annual) for the San Joaquin Valley. The 850 hPa temperatures from the extensive records from San Diego, Oakland, and Vandenberg, along with more limited records from Long Beach (1949–1956), Santa Monica (1956–1965), and Merced (1952–1963, with many gaps), are even more highly correlated, as demonstrated in Table 2. Daily 850 hPa temperature anomalies at San Diego and the Los Angeles stations have a 0.94 (winter) and 0.92 (summer) correlation, and daily anomalies at Oakland and Merced have a 0.94 (winter) and 0.88 (summer) correlation. This clearly demonstrates the applicability of San Diego 850 hPa temperature to the South Coast Basin and the Oakland 850 hPa temperature to the San Joaquin Valley. The daily correlation between San Diego and Oakland is 0.75 (winter) and 0.65 (summer), indicating that 850 hPa temperature patterns are spatially coherent over California. Monthly and annual 850 hPa temperatures produce about the same level of correlations.

Table 1. Maximum/Minimum inter-station θ_{2M} correlations for both daily values and monthly means. Surface temperatures are from available cooperative observer stations within Southern California and the San Joaquin Valley.

	Daily		Monthly	
	NDJF	JJAS	NDJF	JJAS
SC θ_{2M} 00Z	0.89/0.68	0.88/0.54	0.91/0.77	0.84/0.56
SC θ_{2M} 12Z	0.82/0.69	0.79/0.58	0.83/0.76	0.80/0.64
SJV θ_{2M} 00Z	0.90/0.73	0.94/0.83	0.93/0.85	0.90/0.80
SJV θ_{2M} 12Z	0.87/0.72	0.83/0.64	0.92/0.83	0.83/0.50

Note: θ_{2M} is potential temperature at two meters above the surface—a proxy for surface air temperature.

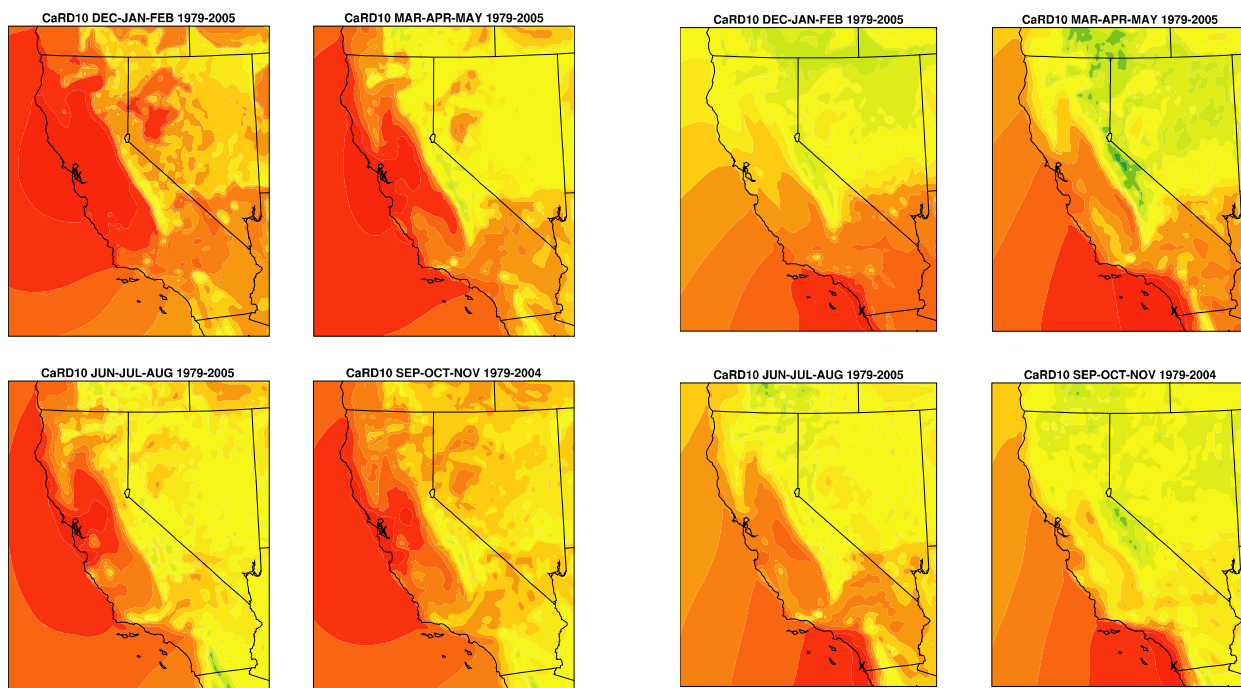
Table 2. Correlations of T_{850} between radiosonde locations for both daily values and monthly means. No overlap (NO) indicates there were less than 30 days in common between a particular station pair.

Daily Values								
	Los Angeles		Vandenberg		Oakland		Merced	
	NDJF	JJAS	NDJF	JJAS	NDJF	JJAS	NDJF	JJAS
San Diego	0.94	0.92	0.88	0.84	0.75	0.65	0.83	NO
Los Angeles			NO	NO	0.82	0.73	0.87	NO
Vandenberg					0.87	0.85	NO	NO
Oakland							0.94	NO
Monthly Means								
	Los Angeles		Vandenberg		Oakland		Merced	
	NDJF	JJAS	NDJF	JJAS	NDJF	JJAS	NDJF	JJAS
San Diego	0.93	0.88	0.92	0.88	0.83	0.73	0.77	NO
Los Angeles			NO	NO	0.85	0.72	0.81	NO
Vandenberg					0.90	0.88	NO	NO
Oakland							0.97	NO

NDJF = November, December, January, February; JJAS = June, July, August, September

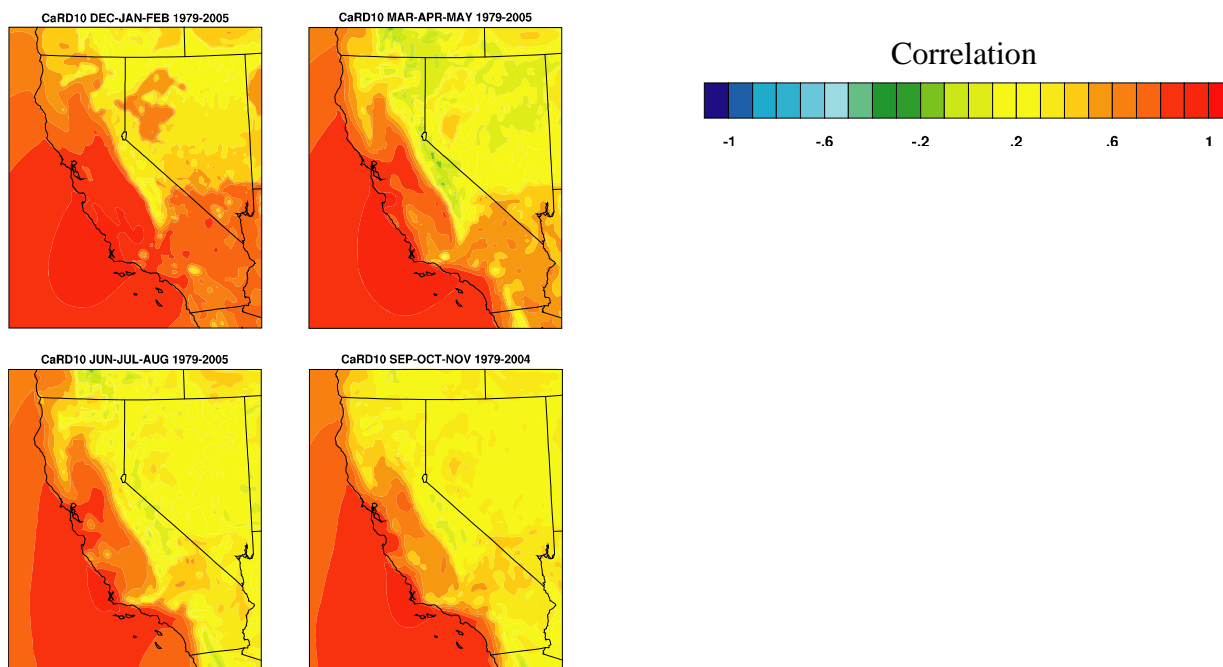
The high-resolution CaRD10 product also provides insight into this question. While a model product, CaRD10 does successfully simulate regional-scale weather patterns such as Santa Ana wind events and Catalina Eddy circulation, thus providing some confidence in the realism of the data. Figure 6 contains the spatial coherence of inversion strength as measured by daily $D\theta_{850}$ values from the CaRD10 data set. These maps were produced by cross-correlating daily $D\theta_{850}$ values at Oakland, Vandenberg, or San Diego to all other grid points.

Relatively strong correlations linking $D\theta_{850}$ at Oakland with $D\theta_{850}$ in neighboring areas are observed, to varying degrees, in all seasons. These strong correlations extend along the northern and central California coastal areas as well as into the Sacramento and San Joaquin Valleys. The extension into the interior valleys is strongest during winter and weakest in summer and fall. There is also strong spatial coherence of $D\theta_{850}$ at Vandenberg into the San Joaquin Valley during winter, but it is significantly weaker during the other seasons, compared to $D\theta_{850}$ at Oakland. While the spatial coherence of $D\theta_{850}$ at San Diego is much more limited than at either Oakland or Vandenberg, it does maintain moderate-to-high values in the South Coast air basin during all seasons. Both Oakland and San Diego $D\theta_{850}$ are well correlated with $D\theta_{850}$ variations offshore from these locations. This analysis indicates that radiosonde measurements from Oakland and San Diego are appropriate to infer inversion measures within the San Joaquin Valley and South Coast air basins, respectively. Note that $D\theta_{850}$ is not meaningful in mountainous regions because the surface is near or above the 850 hPa level.



(A) $D\theta_{850}$ Cross-correlation at Oakland

(B) $D\theta_{850}$ Cross-correlation at San Diego



(C) $D\theta_{850}$ Cross-correlation at Vandenberg

Figure 6. Plots showing cross-correlation (spatial coherence) of daily mean values of $D\theta_{850}$ from the CaRD10 product relative to locations at (a) Oakland, (b) San Diego, and (c) Vandenberg

4.2. Large-Scale Circulation Patterns Associated with Strong and Weak Inversions

Geopotential height and vertical velocity fields from NCEP Reanalysis are used to investigate the relationship between the large-scale atmospheric circulation and the magnitude of inversion strength. Daily fields of 700 hPa geopotential height (H700) and 700 hPa vertical velocity (O700) from NCEP Reanalysis were composited for strong and weak inversions. For the 1979–2005 period, the H700 and O700 fields from the 30 days with the strongest and weakest inversion strengths with respect to the monthly mean were averaged to produce composite plots for the summer and winter seasons. Values of $D\theta_{850,SJV}$ and $D\theta_{850,SC}$ were used as the measure of inversion strength. Note that weak positive values of $D\theta_{850,SJV}$ and $D\theta_{850,SC}$ could occur when no increase in actual temperature with height (e.g., a recognized temperature inversion) exists. In fact, this is an advantage of using $D\theta_{850}$ in this application as it provides a continuous measure of inversion conditions spanning from extremely strong to extremely weak cases. The composite plots for SJV and SC air basins are shown in Figures 7 and 8, respectively.

30-Day Composites Based on Strongest and Weakest SJV 12Z $D\theta_{850}$

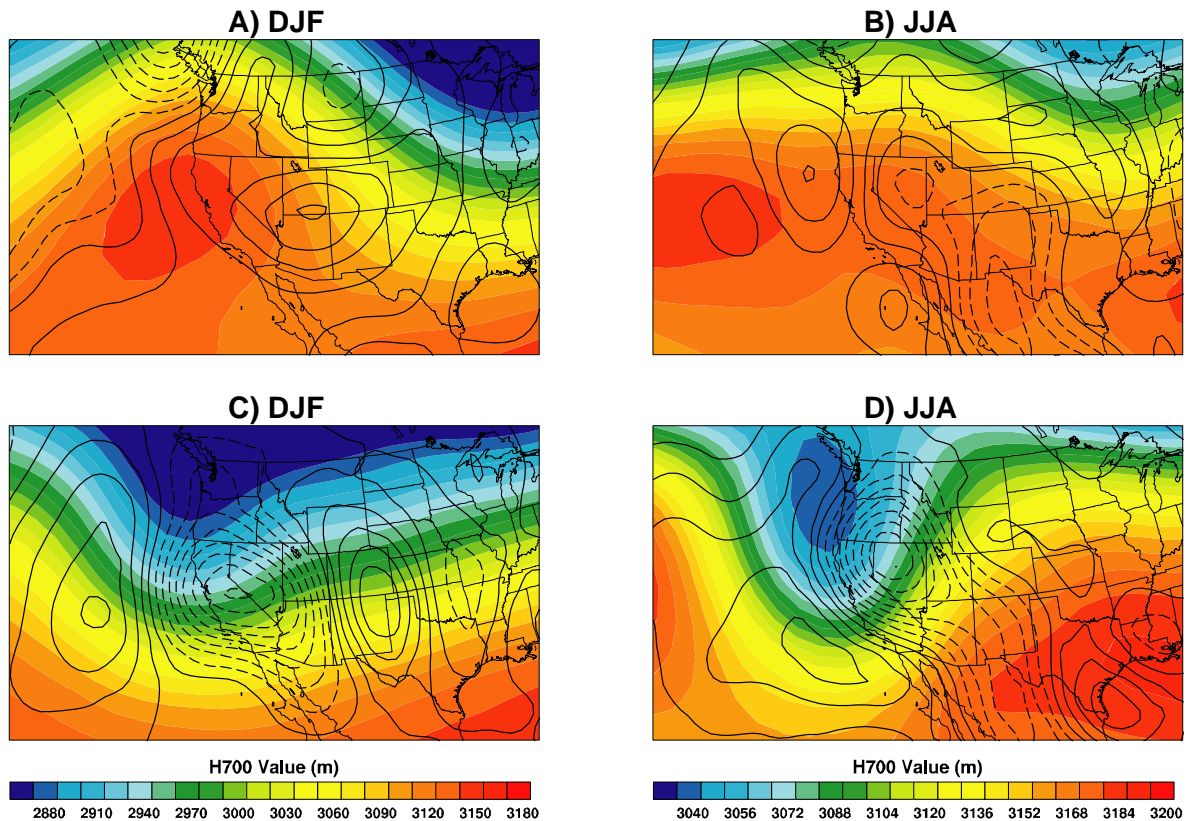


Figure 7. Mean geopotential height and vertical velocity at 700 hPa from NCEP Reanalysis product during the 30 days with the largest (a, b) and smallest (c, d) inversion magnitudes ($D\theta_{850,SJV}$ at 12Z) at SJV during the period 1979–2005. The geopotential heights are shown by the color contours and the vertical velocities are denoted by the black contour lines. Contour intervals are 2 pascals per second (Pa sec^{-1}) (JJA [June, July, August]) and 3 Pa sec^{-1} (DJF [December, January, February]), and dashed contours indicate negative (upward) vertical velocity.

30-Day Composites Based on Strongest and Weakest South Coast 12Z D θ_{850}

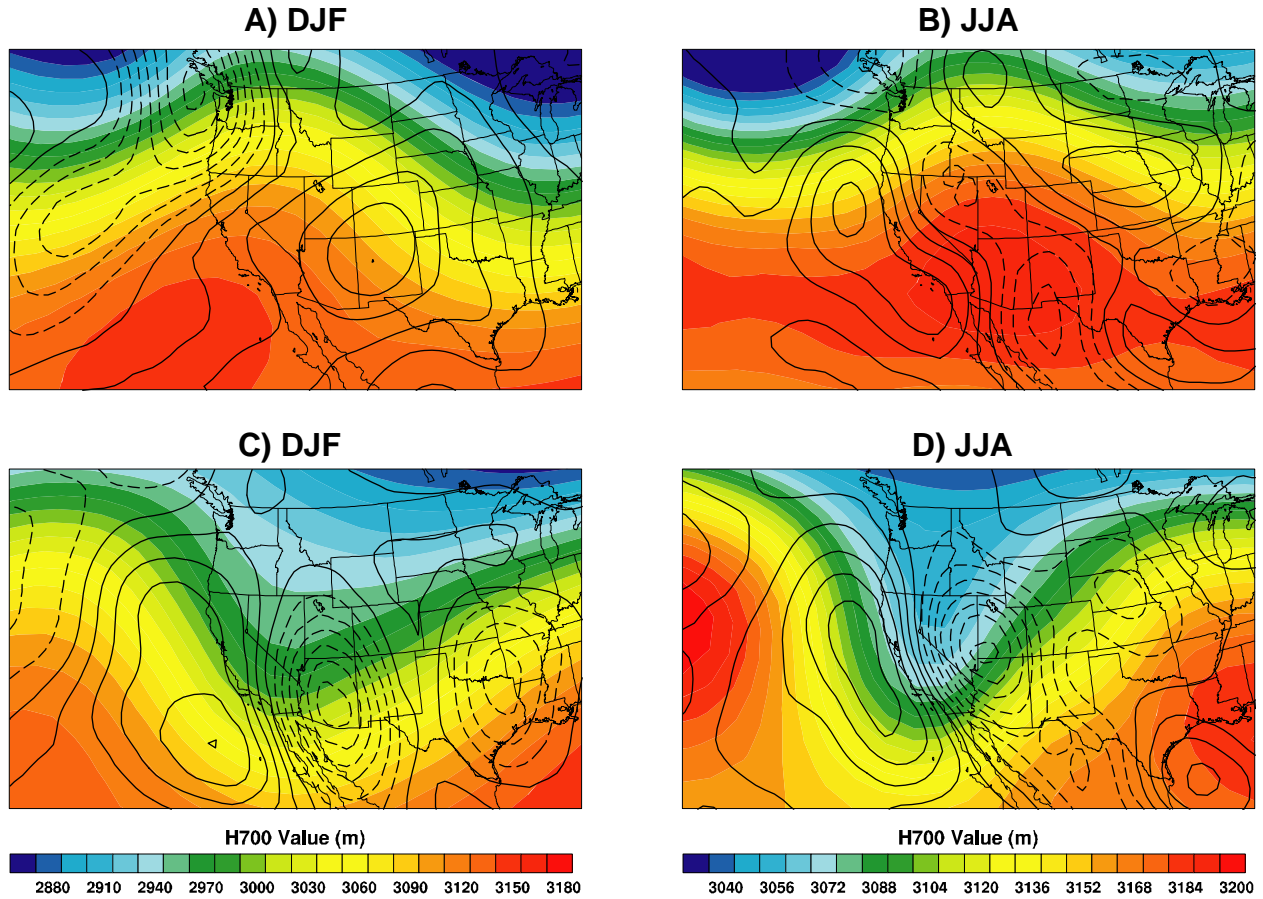


Figure 8. Mean geopotential height and vertical velocity at 700 hPa from NCEP reanalysis during the 30 days with the largest (a, b) and smallest (c, d) inversion magnitudes ($D\theta_{850,SC}$ at 12Z) at the South Coast air basin during the period 1979–2005. The geopotential heights are shown by the color contours, and the vertical velocities are denoted by the black contour lines. Contour intervals are 2 Pa sec⁻¹ (JJA) and 3 Pa sec⁻¹ (DJF) and dashed contours indicate negative (upward) vertical velocity.

From these composites it is clear that quite distinct large-scale atmospheric circulation patterns are associated with strong and weak low-level inversions in California. In general at both locations in both seasons, strong (weak) inversions are associated with an upper-level ridge (trough) at 700 hPa and 500 hPa (not shown). O700 is downward (positive) for strong inversions and upward for weak inversions. Winter season H700 and O700 patterns are generally stronger and of larger horizontal extent than their summer counterparts. Analysis of the anomaly patterns (not shown) shows that during both seasons, the center of the high H700 anomaly pattern is centered slightly to the north of the air basin in question. During winter this area on the southern flank of the height anomaly appears to have some of the largest O700 anomalies.

Composites of regional 10-meter wind from CaRD10 were made using the same procedure as described above. The 10-meter wind composites for the SJV air basin are shown in Figure 9.

During winter, strong inversions in the SJV air basin are associated with quite strong easterly downslope winds over the east side of the valley (foothills of the Sierra Mountains). Within much of the SJV there are generally light winds with a slight anticyclonic (clockwise) circulation along the southern perimeter of the valley. The light winds allow increased surface longwave cooling during the night, aiding the daytime inversion strength. The 10-meter winds off the coast of Central California are generally northeasterly, grading to easterly winds along the coast to the south. Throughout the SJV there are large and consistent values of $D\theta_{850}$, e.g., strong inversions, that extend north into the San Francisco Bay Area and Sacramento Valley during strong SJV winter inversion cases.

Strong summer SJV inversions are associated with moderate northwesterly 10-meter winds throughout most of the SJV, with reduced velocities at the southern end. Winds over the coastal waters of Central California are northwesterly in contrast to the more northerly or northeasterly directed winds during winter. Inspection of the anomalous wind fields (not shown) indicates that the anomalous winds in the SJV and the winds offshore along the California coast are from the southeast, opposing the normal northwesterly wind flow. The overall lower 10-meter winds in the SJV during strong summer inversions would tend to promote more accumulation of pollutants than during conditions associated with normal inversions, further increasing the likelihood of poor air quality. Additionally, the convergence in the southern part of the SJV could facilitate the accumulation of pollution in this area. Values of $D\theta_{850}$ are moderately high and relatively consistent throughout much of Central California, although they are weaker in magnitude than during wintertime. Probably this is because strong summer inversions usually occur when there are extremely warm surface temperatures, while strong inversions during winter often contain relatively cool surface temperatures.

In sharp contrast to the strong inversion composite, weak SJV inversions during winter are associated with southwesterly 10-meter winds throughout much of Central California. These events are most likely related to passing synoptic storm systems with the slight change in direction in the SJV due to interaction of the wind field with the topography of the Coast Ranges and Sierras. During weak winter inversions in the SJV, $D\theta_{850}$ values are much lower throughout the SJV, extending consistently into the Sacramento Valley and into the San Francisco Bay Area. During summer, weak SJV inversions are associated with strong westerly component in the winds off the coast and have a similar pattern of low $D\theta_{850}$ values throughout the Central Valley and into the San Francisco Bay Area. These summer weak inversion cases may also be related to passing synoptic systems.

Figure 10 shows the 10-meter wind composites for the SC air basin. During strong inversions in winter, strong northeasterly 10-meter winds are seen throughout the SC air basin and have the appearance of a Santa Ana wind event. Contrastingly, weak inversion events in winter are associated with moderate north-to-northwesterly winds over most of the SC air basin. Winds over the adjacent coastal waters are also northwesterly and are larger in magnitude. As in the case for the SJV, wintertime weak inversion events are likely related to passing synoptic systems (as suggested by the 700 hPa composite) and are the major control of inversion strength during the winter.

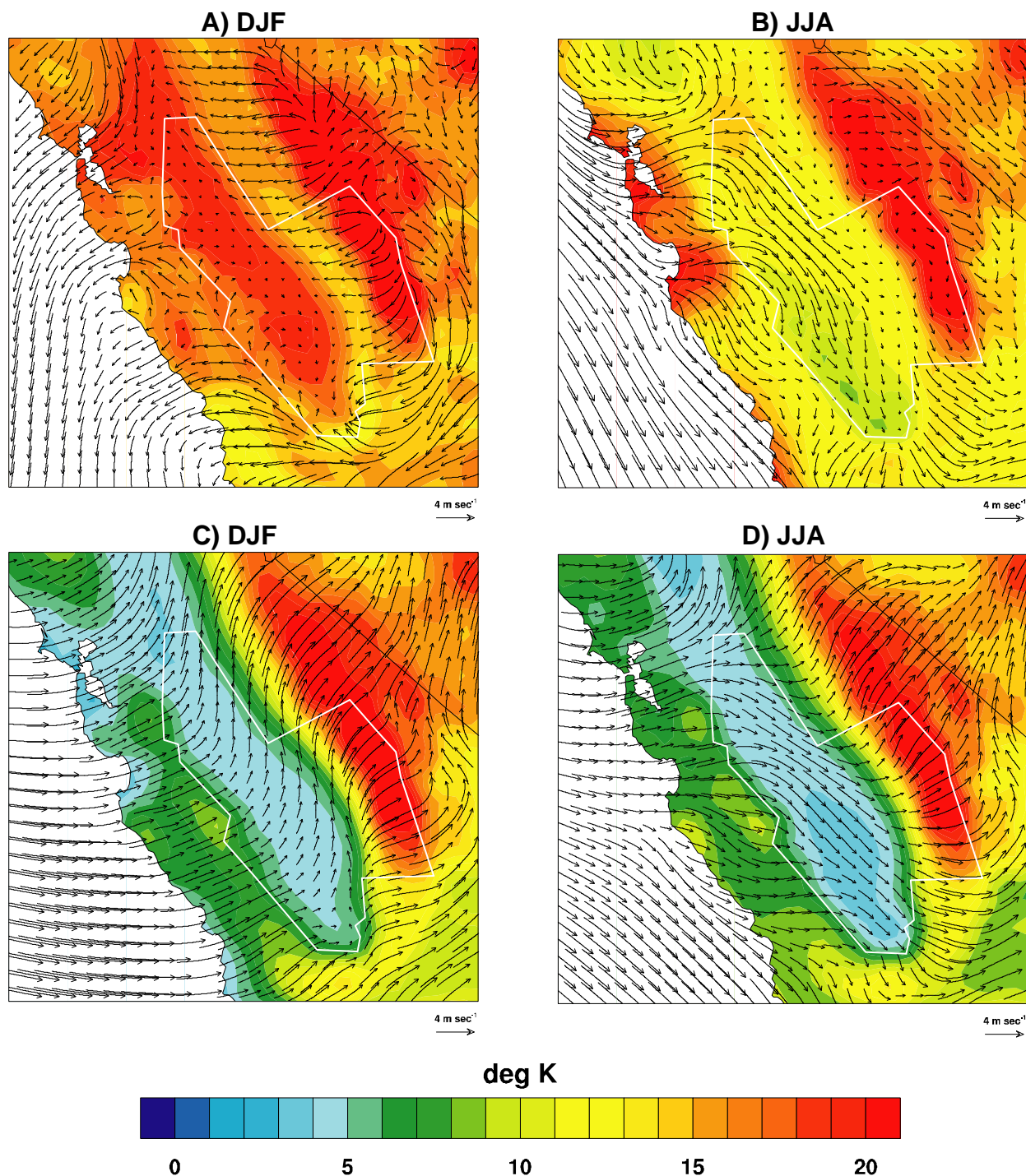


Figure 9. Average values of CaRD10 $D\theta_{850}$ and 10-meter wind during the 30 days with the largest (a, b) and smallest (c, d) observed $D\theta_{850,SJV}$ during time period 1979–2005 for DJF (left column) and JJA (right column). The white line denotes the approximate boundary of the San Joaquin Air Basin. The color filled contours indicate the CaRD10 $D\theta_{850}$ values; the vector arrows represent the 10-meter winds.

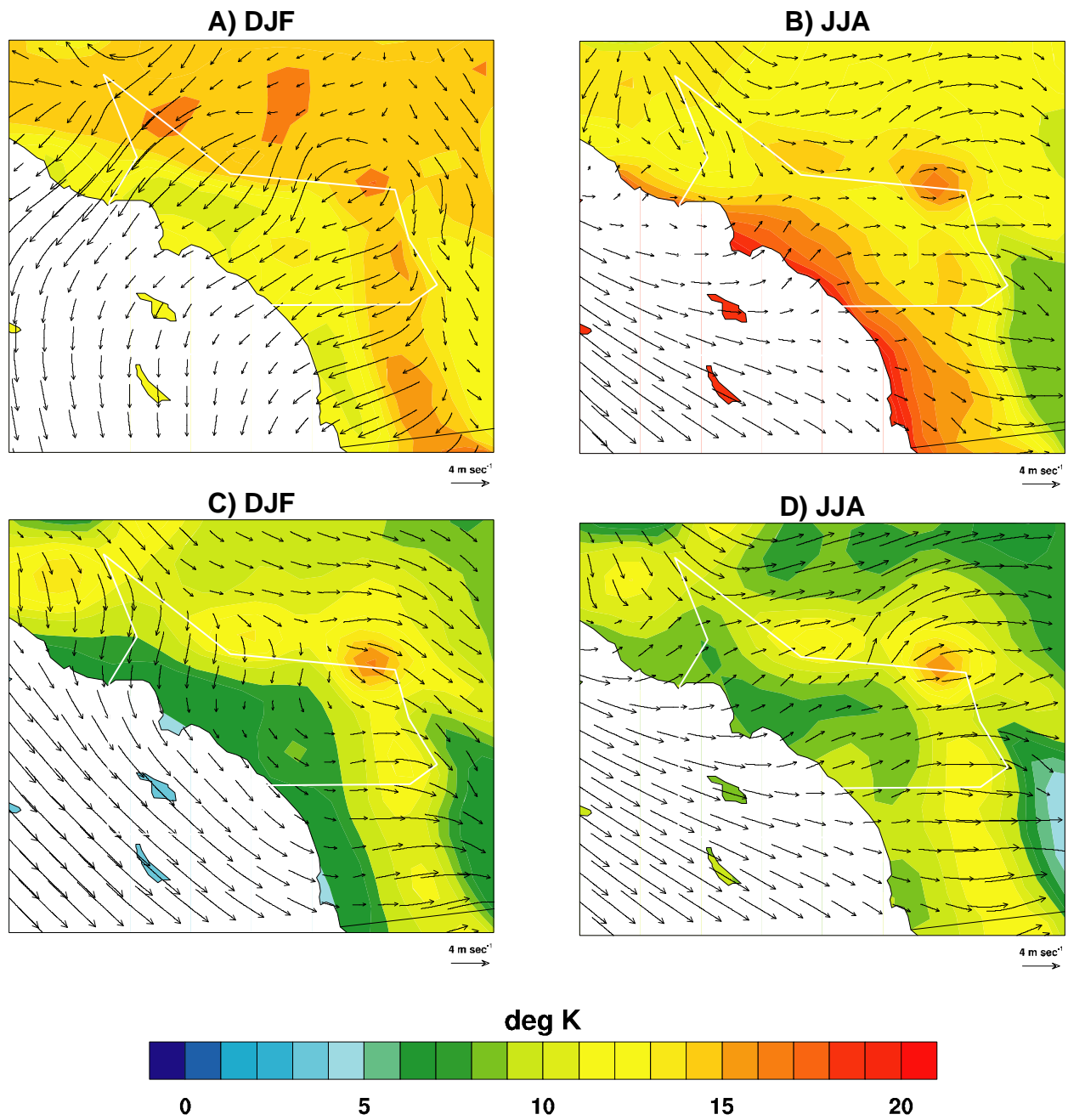


Figure 10. Average values of CaRD10 $D\theta_{850}$ and 10-meter wind during the 30 days with the largest (a, b) and smallest (c, d) observed $D\theta_{850,SC}$ during time period 1979–2005 for DJF (left column) and JJA (right column). The white line denotes the approximate boundary of the South Coast Air Basin. The color filled contours indicate the CaRD10 $D\theta_{850}$ values while the vector arrows represent the 10-meter winds.

During summer, there is less difference in wind direction between strong and weak inversion events over the SC air basin. In both cases, winds over coastal waters are northwesterly and onshore. Examination of wind anomalies (not shown), indicates that weak inversion events have stronger winds with a more westerly component than strong inversion events. Relatively weak values of $D\theta_{850}$ are seen along the coastal areas, which is in strong contrast to the strong inversion case. Since the overall surface circulation pattern is similar in summer for both strong and weak inversions due to the dominance of the summertime North Pacific High, the larger-scale flow at 850 hPa looks to be the primary driver of inversion strength variability. As seen in Figure 8, there are generally low (high) 700 hPa heights over much of Southern California during weak (strong) inversions, which would tend to lead to cooler (warmer) than normal 850 hPa temperatures and reduced (increased) values of $D\theta_{850}$.

4.2.1. Physical Mechanisms and Inversion Characteristics

At the most fundamental level, temperature inversions will be strengthened if heating of the atmosphere above the inversion is greater than heating of the boundary layer and surface below it, or if cooling of the atmosphere above the inversion is less than cooling below. Inversions are weakened if the opposite relative differences in heating/cooling occur. Several mechanisms contribute to heating/cooling, including radiative flux divergence, surface fluxes, and advection. Note that the strength of the inversion is defined as a difference of temperature between the top and the bottom of the inversion layer.

Radiatively driven surface fluxes are clearly responsible for the diurnal cycle in inversion strength over land but also play a role at longer time scales. Greater surface radiative cooling at night will strengthen the surface inversion and may result in a stronger subsidence inversion layer the following day. Greater surface radiative heating during the day will contribute to the weakening of the inversion by increasing the temperature of the boundary layer, but this may be opposed by entrainment growth of the boundary layer that leads to a higher, but stronger inversion. An imbalance between nighttime radiative cooling and daytime radiative heating may lead to a diurnal mean change in inversion strength.

The ocean greatly minimizes radiatively driven variations in surface and boundary layer temperature and thus acts as an anchor for the potential temperature of inversion base. Since the ocean off the coast of California is so cold, there is a strong decrease in inversion strength going inland, especially on days of strong inversions (summertime Figures 9 and 10). All else the same, advection of the marine layer inland will bring cooler boundary layer air to a location and thus strengthen the inversion there. Because hot inland surface temperatures promote the sea breeze, the cooling effect of the marine layer may act as a negative feedback and resist weakening of the inversion. The fact that onshore winds are relatively weaker when the temperature inversion is stronger (summertime Figures 9 and 10) indicates that the sea breeze does not make a substantial contribution to variability in regional inversion strength at synoptic time scales.

Another mechanism for driving temperature changes is horizontal and vertical temperature advection and adiabatic warming associated with large-scale circulation patterns. The geopotential height patterns associated with strong and weak inversions noted in the preceding

section indicate the importance of large-scale circulation on inversions in California. However, these large-scale patterns do not specifically identify the actual physical mechanisms that strengthen or weaken inversions. In this section, NCEP Reanalysis products are further analyzed to help answer this question. We also examine the relative roles of mid-tropospheric and surface processes in driving temperature inversions at synoptic time scales.

Correlations between anomalies of $D\theta_{850}$, θ_{850} , and θ_{2m} for SC and SJV air basins were calculated to see whether an increase in free-tropospheric temperature or a decrease in surface temperature contributed most to inversion strength. On daily to monthly time scales in all cases, the magnitudes of positive correlations between θ_{850} and $D\theta_{850}$ were substantially larger than the magnitudes of negative correlations between θ_{2m} and $D\theta_{850}$. In fact, θ_{2m} was often positively correlated with θ_{850} and $D\theta_{850}$ and frequently exhibited the highest correlation when surface temperature lagged 850 hPa temperature by a day. These results indicate that mid-tropospheric processes are primarily responsible for driving variability in temperature inversions on sub-seasonal time scales. The presence of anomalously cold surface temperature may aid the early development of a strong temperature inversion, but as the inversion continues to evolve, surface temperature warms in response to warming in the free troposphere and thus acts to mute the strength of the temperature inversion.

An examination of temperature variance at standard pressure levels in the San Diego and Oakland soundings indicated that the 850 hPa level experienced larger changes in daily temperature than any other pressure level. Additionally, the 850 hPa level is the standard pressure that is most commonly located immediately above the inversion top and would be most indicative of how the free atmosphere impacts the inversion layer. Thus, the mechanism(s) driving variations in 850 hPa temperature must also be primarily responsible for producing strong temperature inversion events. Since radiative and turbulent processes act on somewhat long time scales (relative to a few days) in the free troposphere, we assume that advection is one of the principal drivers of 850 hPa temperature on synoptic time scales.

To test this hypothesis, finite differences were applied to the NCEP reanalysis to calculate horizontal potential temperature advection, vertical potential temperature advection, and the local rate of potential temperature change at 850 hPa and 1000 hPa for grid points near San Diego and Oakland. Total (horizontal + vertical) advection of potential temperature is correlated with the local rate of potential temperature change at values of 0.54–0.67 for both the cool and warm seasons and at both San Diego and Oakland (positive advection value indicates warming). These correlations are likely biased low due to errors resulting from the crudeness of finite difference calculations on standard pressure levels and by the lack of energy conservation in the NCEP reanalysis. Furthermore, horizontal and vertical advection are substantially anti-correlated at both locations, which would mean that the total is to some extent a difference between large quantities and thus more susceptible to the errors noted above. Correlations between horizontal and vertical advection were -0.65 and -0.75 during the cool season and -0.40 and -0.48 during the warm season, with the correlations at Oakland larger than at San Diego. The larger anti-correlation at Oakland during both seasons is probably due to the closer proximity to the storm track resulting in more frequent and stronger influences from synoptic storm systems. At both San Diego and Oakland, variability in vertical advection dominates

horizontal advection in contributing to variability in total advection during winter but contributes equally with horizontal advection to variability in total advection during summer.

The compensation between horizontal and vertical advection is a key issue for understanding 850 hPa temperature change. Subsidence causes warming at 850 hPa because air with higher potential temperature has moved down to replace air with lower potential temperature. Quasi-geostrophic dynamics, however, causes this downward motion to be associated with horizontal cold advection, which cancels much or all of the vertical warm advection. In particular, a local maximum in subsidence is typically not associated with the greatest local warming, as seen in Figures 7 and 8, because horizontal cold advection is also large there. Neither does the greatest local warming occur under the peak elevation of an upper-level ridge, since subsidence is typically weak there (Figures 7 and 8). The favorable conditions are instead the particular combination of vertical warm advection that is relatively strong and horizontal cold advection that is relatively weak. For example, subsidence is strong in the cold sector following the passage of a surface front and upper-level trough, but horizontal cold advection overwhelms vertical warm advection, so such conditions do not contribute in the composite plots. The strongest wintertime inversions are instead associated with northeasterly Santa Ana-like flow (Figures 9 and 10).

Key variables from the NCEP Reanalysis product were composited for the 30 days with the strongest inversions. Two composites were made again using values of $D\theta_{850,SJV}$ and $D\theta_{850,SC}$ as the measure of inversion strength. Each composite was calculated at the closest Reanalysis grid point to the appropriate site. Additionally, the composites extend 10 days prior to and 10 days after the day with maximum $D\theta_{850}$, allowing the investigation of the temporal evolution and interaction of various physical processes.

We found that at both locations in both seasons, vertical warm advection transitions from being smaller to being larger than horizontal cold advection at 850 hPa several days prior to maximum $D\theta_{850}$. Potential temperature at 850 hPa thus begins increasing and hence $D\theta_{850}$ becomes stronger. Immediately following maximum $D\theta_{850}$, subsidence and vertical advection weaken and become smaller than horizontal cold advection. This causes $D\theta_{850}$ to decrease, along with a contribution from increasing θ_{2m} . During winter, the pattern of advection at 1000 hPa is generally similar to the pattern at 850 hPa, but during summer strong inversion cases total advection at 1000 hPa always acts to cool, due to the weakness of vertical motion near the surface and the strength of prevailing horizontal cold advection. The observed warming of summertime θ_{2m} is likely instead driven by radiative heating, which can be strong near the surface.

For strong inversion cases in winter and summer in the SC air basin and in winter in the SJV, the increase in warm total advection several days prior to maximum $D\theta_{850}$ is driven by a strengthening of subsidence, but for the summertime SJV, it is instead caused by a weakening of horizontal cold advection. Weaker than average horizontal cold advection, however, is a precondition necessary for the development of strong inversion events during summer in the SC basin and SJV, as is suggested by Figures 9 and 10.

4.3. Impact of Local Sea Surface Temperature on Inversion Measures

The proximity of California to relatively cool Pacific sea surface temperatures (SSTs) may play an important role in the strength and variability of inversions in coastal regions. Strong inland surface heating can act to weaken the local inversion strength by increasing the temperature at the inversion base. The strong surface heating often initiates a sea breeze circulation that provides a relatively cool horizontal (onshore) flow near the coast that will tend to cool the inversion base and thereby increase the inversion strength and cancel out at least part of the weakening due to the surface heating. One would expect the impact of the sea breeze on inversion strength to increase as the ocean-land temperature contrast increases, unless particular synoptic conditions act to prevent this, as suggested in Figures 9 and 10. It is important to note that the sea breeze circulation is initiated by the inland surface heating, and as a result acts as a negative feedback to any decreases in inversion strength caused by the surface heating. As a result the sea breeze may help to maintain an inversion, but in general does not increase the strength of an existing inversion.

Table 3 contains correlations between monthly mean values of local SST and inversion measures DT_{INV} , DZ_{INV} , $D\theta_{850}$, and θ_{2M} . Local SST is calculated as an average over several $1^\circ \times 1^\circ$ grid cells immediately off the coast and was obtained from the Reynolds OI.v2 SST analysis extending from November 1981 to present (Reynolds et al. 2002). Correlations greater than 0.19 at San Diego and 0.22 at Oakland are significant at the 95% confidence level. Significance levels of the data in Table 3 were determined using decorrelation times based on the e-folding time of the autocorrelation function.

Significant anti-correlations exist between SST and inversion strength (as measured by either DT_{INV} or $D\theta_{850}$), indicating that cooler SSTs are associated with stronger and thicker inversions. The low correlation of $D\theta_{850,SJV}$ is due to a reduced influence of local SST on the near surface temperatures in the San Joaquin Valley compared to the South Coast air basin. Relative to the South Coast air basin, the San Joaquin Valley is physically further away from the ocean. Additionally, most of the western edge of the SJV is bounded by the Coast Ranges acting as a significant topographic boundary inhibiting surface level flow between the Pacific Ocean and the valley.

Multiple linear regression analysis was used to help isolate the impact of the local SST from any possible effects of either the El Niño/Southern Oscillation (ENSO) or the Pacific Decadal Oscillation (PDO). An initial linear regression was performed using the Southern Oscillation Index (SOI) and PDO indices as predictors and DT_{INV} as the predictand. Lead times of two months for SOI and 1 month for PDO were used to produce a regression that explained a maximum amount of variance. An additional regression, now using local SST in addition to the SOI and PDO indices, explained 50% more variance than did the initial regression, indicating that the local SST adds a significant amount of information to this relation. SST probably contributes more to inversion variability on monthly and longer time scales as atmospheric synoptic variations tend to average out.

Table 3. Correlations between monthly mean values of local SST and various inversion measures at Oakland and San Diego. Correlations greater than 0.19 at San Diego and 0.22 at Oakland are significant at the 95% confidence level.

Inversion Measure	San Diego	Oakland
DT_{INV}	-0.37	-0.33
DZ_{INV}	-0.33	-0.30
$D\theta_{850,SJV}$	—	-0.05
$D\theta_{850,SC}$	-0.31	—
$\theta_{2M,SJV}$	—	0.06
$\theta_{2M,SC}$	0.34	—

4.4. Temporal Variations of Inversion Measures

4.4.1. Time Series of Inversion Strength and Inversion Depth

To investigate how inversions may vary on interannual and multi-year time scales, time series of monthly mean DT_{INV} , DZ_{INV} , and Z_{BASE} anomalies were constructed from radiosonde measurements at Oakland and San Diego. Additionally, time series of monthly mean $D\theta_{850,SJV}$ and $D\theta_{850,SC}$ anomalies were made using the radiosonde data and surface temperature measurements in the San Joaquin Valley and South Coast air basins. These time series are shown in Figure 11 (Oakland/SJV) and Figure 12 (San Diego/SC). The monthly means shown in these figures only include data for subsidence inversions ($Z_{BASE} > 50$ m). Radiation inversions are examined separately below. The monthly mean anomalies were calculated using monthly climatologies computed from the entire 1960–2007 period.

The time series in figures 11 and 12 all contain significant interannual and decadal variability. To determine if these fluctuations are linked to large-scale fluctuations in Pacific climate, correlations between DT_{INV} and DZ_{INV} versus the ENSO and the PDO were computed, shown in Table 4. Annual mean values of DT_{INV} and DZ_{INV} were calculated using only those days when a subsidence inversion was present; days with radiation inversions were not included. The ENSO variations were represented by the SOI and by the Niño 3.4 SST, and the PDO was represented the leading principal component of monthly SST anomalies in the North Pacific Ocean poleward of 20°N, as derived by Zhang et al (1997).¹ A twelve-month running mean filter was applied to all time series. Correlations were calculated using a lead time of 1 month for ENSO and 2 months for SOI and Niño 3.4 SST. Correlations greater than 0.28 are significant at the 95% confidence level.

¹ Available online at <http://jisao.washington.edu/pdo/>.

Oakland/SJV Subsidence Inversions

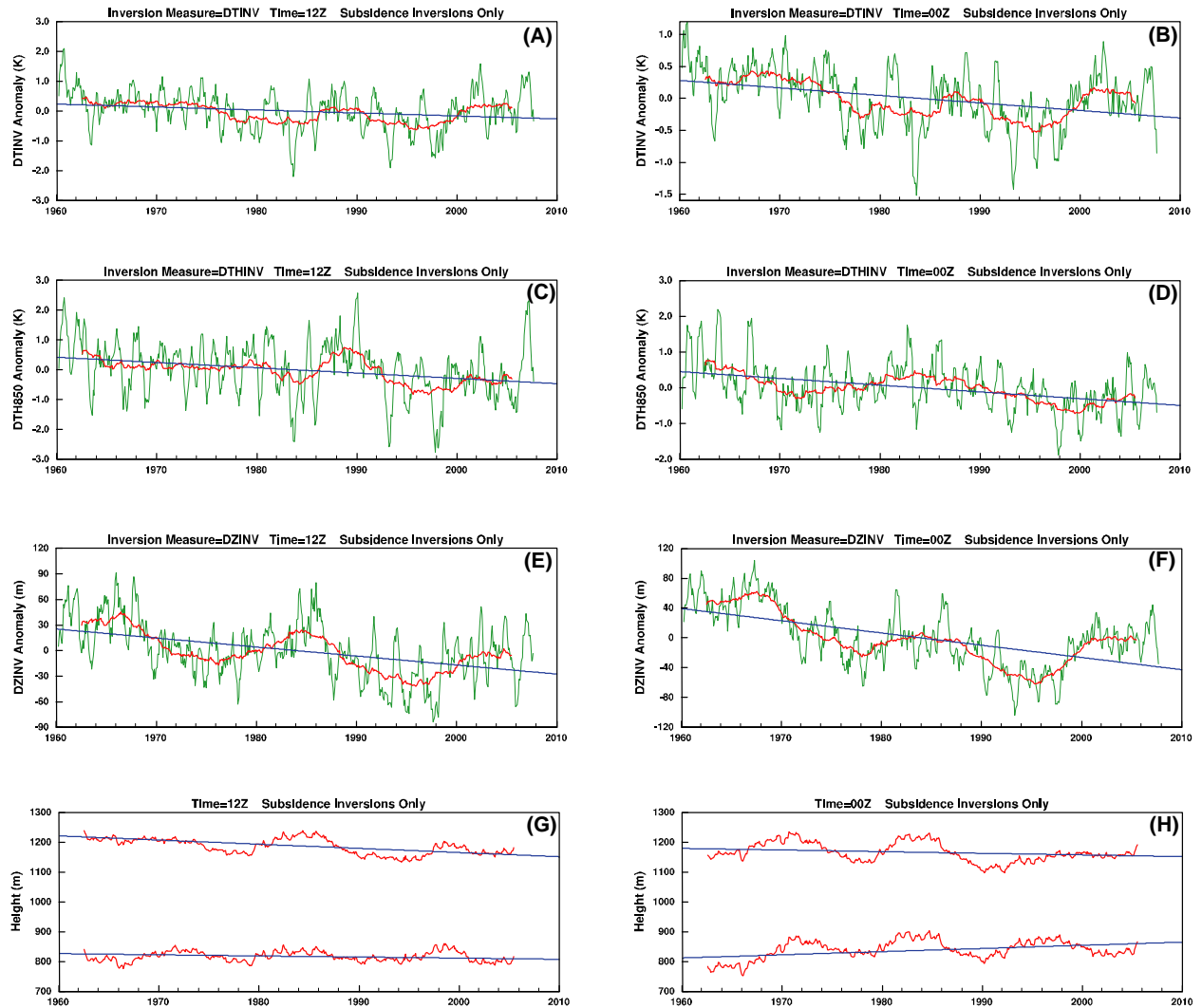


Figure 11. Time series of filtered monthly mean values of (a) 12Z DT_{INV} , (b) 00Z DT_{INV} , (c) 12Z $D\theta_{850,SJV}$, (d) 00Z $D\theta_{850,SJV}$, (e) 12Z DZ_{INV} , (f) 00Z DZ_{INV} , (g) 12Z Z_{TOP} and Z_{BASE} , and (h) 00Z Z_{TOP} and Z_{BASE} based on the Oakland radiosonde data and surface temperature measurements in the San Joaquin Valley air basin. For each variable a six-month running mean (green line) and a five-year running mean filter (red line) are shown except for the bottom row of plots showing Z_{TOP} and Z_{BASE} , where only the five-year running mean filtered data is shown for clarity. The straight blue lines represent a linear best fit to the data. The monthly means were calculated using only days when subsidence inversions were observed.

San Diego/SC Subsidence Inversions



Figure 12. Time series of filtered monthly mean values of (a) 12Z DT_{INV}, (b) 00Z DT_{INV}, (c) 12Z D_θ_{850,SC}, (d) 00Z D_θ_{850,SC}, (e) 12Z DZ_{INV}, (f) 00Z DZ_{INV}, (g) 12Z Z_{TOP} and Z_{BASE}, and (h) 00Z Z_{TOP} and Z_{BASE} based on the San Diego radiosonde data and surface temperature measurements in the South Coast air basin. For each variable a six-month running mean (green line) and a five-year running mean filter (red line) are shown, except for the bottom row of plots showing Z_{TOP} and Z_{BASE} where only the five-year running mean filtered data is shown for clarity. The straight blue lines represent a linear best fit to the data. The monthly means were calculated using only days when subsidence inversions were observed. Note: Data gaps in some of the filtered data curves are due to some months with no subsidence inversions.

Table 4. Correlation between 1960–2007 filtered monthly means: Inversion measures vs. SST indices. Monthly means of the inversion measures are for subsidence inversions only. The time series were detrended and then filtered using a 12-month running mean. Correlations greater than 0.28 are significant at the 95% confidence level.

		PDO Index	SOI Index	Niño 3.4
Oakland				
	DT _{INV} 00Z	-0.43	+0.34	-0.24
	DZ _{INV} 00Z	-0.29	+0.20	-0.13
	DT _{INV} 12Z	-0.43	+0.33	-0.25
	DZ _{INV} 12Z	-0.10	+0.12	-0.18
San Diego				
	DT _{INV} 00Z	-0.49	+0.51	-0.40
	DZ _{INV} 00Z	-0.54	+0.40	-0.33
	DT _{INV} 12Z	-0.58	+0.51	-0.43
	DZ _{INV} 12Z	-0.42	+0.45	-0.40

Although inversion measures of DT_{INV} and DZ_{INV} are not real strongly associated with ENSO, there are significant correlations (Table 4). Stronger and thicker inversions are positively correlated with the SOI Index and negatively correlated with the Niño 3.4 SST record, with correlation magnitudes of approximately 0.2–0.5. Thus, during El Niño episodes (warm SST in Central Tropical Pacific and off the California coast), weaker and thinner inversion layers tend to occur in California. The opposite is true during La Niña events, when stronger and thicker inversions occur. The correlations are largest for San Diego, indicating that the ENSO linkage may fade northward along the California coast. Weaker inversions during El Niño episodes appear to be consistent with the tendency for strengthened westerly winds and presumably more frequent synoptic events during these cases. There is a greater tendency for horizontal warm advection during El Niño episodes, which leads to higher surface temperatures on land and the coastal ocean. Vertical cold advection occurs at 850 hPa, leading to relative cooling at that level and consequently weaker inversions. Stronger inversions during La Niñas would likely result from more frequent high-pressure situations and more vertical warm advection during these cases.

There is also a connection to PDO. Table 4 shows significant correlations, up to about -0.6 between these inversion measures and the PDO, at both locations. The sense of these correlations indicates that stronger and thicker inversions occur with the cool phase (relatively cool SST in the eastern Pacific off of North America) of the PDO. This link is consistent with the ENSO correlation results, since the cool phase of PDO is more La Niña-like and the warm phase of PDO is more El Niño-like. Over the available historical period, inversions were stronger and thicker during the cool PDO phase during the 1960s through the mid-1970s and during the recent period after 1998, while they were weaker and thinner during the PDO warm phase that prevailed from the mid-1970s through 1998. Similar to the ENSO results, the correlations between inversion measures and the PDO are stronger at San Diego compared to Oakland.

In addition to having substantial interannual-decadal fluctuations, the inversion characteristics have undergone some notable long-term changes over the period of observations. The change in magnitude (in relative % measure) of several inversion measures during the period 1960–2007 calculated from radiosonde measurements are given in Table 5. Also shown in the table are values of the absolute change in magnitude normalized by the standard deviation of the annual means; these values are included to represent an estimate of the strength or significance of the change. Data is given for both the Oakland and San Diego radiosonde and for both the 00Z and 12Z launch time and are for subsidence-type inversions only. These changes were calculated using a best-fit linear trend through the monthly mean data.

Table 5. Change in magnitude of several inversion measures during the period 1960–2007 calculated from radiosonde measurements. Results are for subsidence-type inversions. The values shown in parentheses are the absolute changes in magnitude normalized by the standard deviation of the annual means for each variable, location, and launch time. Note: $D\theta_{850}$ values were calculated using radiosonde data and surface temperature observations in the San Joaquin Valley and South Coast air basins.

	San Diego 00Z	San Diego 12Z	Oakland 00Z	Oakland 12Z
DT_{INV} (°K)	-0.6 (137%)	-0.6 (104%)	-0.6 (147%)	-0.5 (98%)
DZ_{INV} (°K)	-117 (243%)	-78 (207%)	-79 (210%)	-51 (182%)
Z_{TOP} (m)	-24 (42%)	-65 (102%)	-23 (37%)	-65 (105%)
Z_{BASE} (m)	+93 (150%)	+13 (19%)	+56 (89%)	-15 (25%)
$D\theta_{850}$ (°K)	-0.6 (105%)	-0.7 (91%)	-0.8 (163%)	-0.9 (131%)
T_{TOP} (°K)	+0.3 (44%)	+0.6 (76%)	+0.5 (76%)	+0.8 (118%)
T_{BASE} (°K)	+0.9 (134%)	+1.1 (158%)	+1.1 (159%)	+1.3 (190%)
T_{850} (°K)	+0.6 (119%)	+0.7 (106%)	+0.6 (98%)	+0.7 (107%)
T_{500} (°K)	+0.8 (195%)	+1.1 (174%)	+0.9 (173%)	+0.9 (183%)
$D\theta DZ_{850-500}$ (°K km ⁻¹)	+0.08 (67%)	+0.12 (80%)	+0.09 (69%)	+0.08 (67%)
θ_{TOP} (°K)	+0.1 (23%)	+0.1 (13%)	+0.3 (50%)	+0.2 (28%)
θ_{BASE} (°K)	+1.9 (225%)	+1.4 (173%)	+1.6 (222%)	+1.2 (178%)
θ_{2M}	+1.3 (190%)	+1.5 (211%)	+1.6 (211%)	+1.5 (214%)

Over the 48-year period, inversion strength as measured by DT_{INV} decreased at Oakland by 8% at 12Z and by 16% at 00Z. Comparable decreases in DT_{INV} of 10% at 12Z and 16% at 00Z were observed at San Diego. Separate measures, $D\theta_{850,SJV}$ and $D\theta_{850,SC}$, formed from 850 hPa potential temperature from the radiosonde profiles and surface temperature from clusters of cooperative observer stations, showed changes of similar magnitude. A somewhat fragmentary record from radiosonde observations at Vandenberg Air Force Base also exhibits similar decreases.

Furthermore, the thickness of the inversion layer decreased over this time period. At Oakland, DZ_{INV} decreased by 14% (12Z) and 24% (00Z), while at San Diego decreases of 21% (12Z) and 36% (00Z) were observed. At 12Z, the decreasing inversion layer thickness is mostly due to a lowering of the inversion top, while at 00Z both a lowering inversion top and a rising inversion base were responsible.

The largest change (relative to the normalized values) is seen in the overall inversion thickness. At both Oakland and San Diego, the inversion base during the afternoon (00Z) has become elevated over the 48-year period; this lifting in height was approximately 60 m at Oakland and 90 m at San Diego—an increase over the average base height of 800 m at Oakland and 650 m at San Diego at the beginning of the record. At both Oakland and San Diego, the inversion top height decreased by approximately 65 m at 12Z and 25 m at 00Z.

Temperature increased by 0.9 K–1.3K (1.6°F–2.3°F) at the inversion base while inversion top temperatures increased by 0.3–0.8°K (0.5°F–1.4°F). The larger increase in inversion base temperature resulted in the decreasing trend in DT_{INV} noted earlier. The increases in inversion base temperature also appear to be more significant, based on the relatively large normalized values. Additionally, the soundings consistently show larger temperature increases at the 500 hPa level compared to 850 hPa, which leads to an increased static stability in this region of atmosphere over both Oakland and San Diego. The increasing trend in T_{500} appears to be stronger (both in absolute and normalized terms) than the trend in T_{850} , while the trend in static stability is relatively weaker with respect to the normalized values.

All of the above calculated trends were based on radiosonde measurements (except $D\theta_{850,SJV}$ and $D\theta_{850,SC}$ which were based on both radiosonde and surface temperature measurements) at Oakland and San Diego. A caution in interpreting these trends is that some of these changes may have resulted from time-changing errors and/or biases based on changes in procedures and/or instrumentation. To aid in the application of this information to climate change studies, corrections to global radiosonde data sets have been made by Free et al. (2005) (RATPAC), Thorne et al. (2005) (HadAT2), and Haimberger (2005) (RAOBCORE). Each of these studies used a different and independent methodology to determine the temperature adjustments to remove inhomogeneities. The San Diego radiosonde data was included in all three studies, while the Oakland radiosonde data was included in only two of the studies. Unfortunately, the adjustments only apply to the standard pressure levels and are generally not available between the surface and 850 hPa where the vast majority of low-level temperature inversions are located. For this reason these adjustments were not directly used in the above analysis.

Investigation of trends in the adjusted temperature datasets, however, may provide some insight into the reliability of trends found in Table 5. Each of the adjusted radiosonde data sets yielded similar increasing trends in T_{850} over the 48-year period at San Diego that averaged about 0.2 K (0.4°F) larger than what was found with the original radiosonde data. This would imply that the decreasing trend in $D\theta_{850,SC}$ may be about 0.2 K (0.4°F) too large in magnitude, since the surface temperatures were already subject to a correction procedure. One of the two adjusted radiosonde data sets available for the Oakland site (HadAT2) consistently produced a more positive T_{850} trend than was in the original radiosonde data, and the other (RAOBCORE) consistently produced a more negative trend. This implies that the uncertainty in the Oakland trends is larger than what may be estimated from the original data alone, especially considering that the three data sets did not agree on the sign of the wintertime Oakland T_{850} trend. When combined with the surface data, the three radiosonde data sets indicate that wintertime $D\theta_{850,SJV}$ experienced a trend that was near zero or increasing.

If the adjustments to the radiosonde temperature data are uniform in height below the 850 hPa level, then there would probably be little if any change to the DT_{INV} trends calculated here. Additionally, trends in the thickness of the inversion layer DZ_{INV} would also be minimally affected, since the inflection points in the temperature profile would not change if a continuous temperature adjustment was applied.

Nonetheless, changes to equipment and/or algorithms used to derive radiosonde heights and temperatures could impart artificial trends to the radiosonde heights and temperatures. It is more likely that any artificial trend would affect the calculated trend at a particular level such as inversion base or inversion top. It is less likely that an artificial trend would have a significant impact on the difference between values at two different levels such as DT_{INV} or DZ_{INV} unless there has been a change in sensor response time. Although the radiosonde models examined by Gaffen (1994) were not used in the United States, if the technology was similar, then there are likely to have been no significant changes in sensor response time between the mid 1970s until at least the early 1990s.

As noted earlier in Section 2, the vertical resolution of radiosonde temperature readings between the surface and 700 hPa varied over the time period studied. Tests with a resampled data set providing a constant vertical resolution produce results with the same qualitative trends in DT_{INV} and DZ_{INV} , except for the 12Z DZ_{INV} at San Diego which showed no significant change over the 48-year period. The impact of variable vertical resolution throughout the time period should have little or no impact on the variables $D\theta_{850}$ since the 850 hPa level is a standard reporting level that is included in all the original radiosonde reports.

Correlations between the various inversion measures are useful to interpret the changes represented in Table 5 and elsewhere. Correlations between various inversion measures are displayed in Tables 6–9 for both daily values and monthly means. These correlations were calculated using only days when a subsidence inversion was measured with the resulting time series detrended. Results are presented at the 00Z launch time to maximize the occurrence of subsidence-type inversions to prevent biases in monthly means. Several of the measures are strongly correlated ($r > 0.5$, $p < 0.01$). These include a strong positive correlation between DT_{INV} and DZ_{INV} on monthly time scales, indicating that stronger/weaker inversions are also thicker/thinner in vertical extent. Strong anti-correlations exist for the temperature and height at the base and top of the inversion layer for both daily and monthly time scales. Additionally, T_{TOP} and T_{BASE} are strongly correlated with T_{850} and to a lesser extent with T_{500} . In general, the correlations between the various temperatures decrease as the physical distance between the locations increase. The thickness of the inversion is not significantly correlated with either Z_{TOP} or Z_{BASE} , a reflection of the two height measures being so strongly correlated, and thus the difference was not too well correlated with either measure. The stability of the atmospheric layer between 850 hPa and 500 hPa is strongly correlated to T_{850} , but weakly correlated with T_{500} . This perhaps indicates that the dynamics driving the temperatures at the 850 hPa level are more relevant to low-level temperature inversions in California than the dynamics at 500 hPa.

Table 6. Correlation of daily values from 1960–2007 Oakland 00Z radiosonde measurements. The correlations were calculated using only days when a subsidence inversion was observed in the radiosonde data. The various time series were detrended prior to calculation.

	DT _{INV}	DZ _{INV}	Z _{TOP}	Z _{BASE}	Dθ ₈₅₀	T _{TOP}	T _{BASE}	T ₈₅₀	T ₅₀₀	DθDZ ₈₅₀₋₅₀₀	θ _{TOP}	θ _{BASE}	θ _{2M}
DT _{INV}	1.00												
DZ _{INV}	0.46	1.00											
Z _{TOP}	-0.08	0.16	1.00										
Z _{BASE}	-0.25	-0.21	0.93	1.00									
Dθ _{850,SJV}	0.34	0.27	-	-0.45	1.00								
T _{TOP}	0.38	0.19	-	-0.79	0.58	1.00							
T _{BASE}	-0.08	-0.02	-	-0.73	0.46	0.89	1.00						
T ₈₅₀	0.45	0.29	-	-0.61	0.68	0.91	0.76	1.00					
T ₅₀₀	0.18	0.16	-	-0.29	0.38	0.55	0.50	0.60	1.00				
DθDZ ₈₅₀₋₅₀₀	-0.38	-0.20	0.41	0.48	-0.48	-	-0.46	-	0.21	1.00			
θ _{TOP}	0.43	0.47	0.31	0.14	0.32	0.42	0.24	0.59	0.45	-0.30	1.00		
θ _{BASE}	-0.44	-0.31	0.28	0.39	-0.01	0.11	0.34	0.19	0.28	0.03	0.53	1.00	
θ _{2M}	0.28	0.12	-	-0.38	-0.07	0.66	0.58	0.68	0.44	-0.42	0.48	0.27	1.00

Table 7. Correlation of monthly means from 1960–2007 Oakland 00Z radiosonde measurements. The monthly means were calculated using only those days when a subsidence inversion was observed in the radiosonde data. The various time series were detrended prior to calculation.

	DT _{INV}	DZ _{INV}	Z _{TOP}	Z _{BASE}	Dθ ₈₅₀	T _{TOP}	T _{BASE}	T ₈₅₀	T ₅₀₀	DθDZ ₈₅₀₋₅₀₀	θ _{TOP}	θ _{BASE}	θ _{2M}
DT _{INV}	1.00												
DZ _{INV}	0.70	1.00											
Z _{TOP}	-0.24	0.03	1.00										
Z _{BASE}	-0.46	-0.36	0.94	1.00									
Dθ _{850,SJV}	0.47	0.46	-	-0.48	1.00								
T _{TOP}	0.52	0.37	-	-0.83	0.53	1.00							
T _{BASE}	0.12	0.10	-	-0.74	0.38	0.91	1.00						
T ₈₅₀	0.55	0.43	-	-0.71	0.57	0.96	0.85	1.00					
T ₅₀₀	0.28	0.33	-	-0.38	0.36	0.65	0.62	0.71	1.00				
DθDZ ₈₅₀₋₅₀₀	-0.48	-0.26	0.57	0.61	-0.44	-	-0.56	-	0.04	1.00			
θ _{TOP}	0.52	0.53	-	-0.19	0.40	0.67	0.52	0.77	0.66	-0.40	1.00		
θ _{BASE}	-0.42	-0.33	0.14	0.25	-0.08	0.23	0.47	0.30	0.40	-0.01	0.51	1.00	
θ _{2M}	0.23	0.10	-	-0.42	-0.22	0.67	0.67	0.67	0.52	-0.41	0.56	0.43	1.00

Table 8. Correlation of daily values from 1960–2007 San Diego 00Z radiosonde measurements. The correlations were calculated using only days when a subsidence inversion was observed in the radiosonde data. The various time series were detrended prior to calculation.

	DT _{INV}	DZ _{INV}	Z _{TOP}	Z _{BASE}	Dθ ₈₅₀	T _{TOP}	T _{BASE}	T ₈₅₀	T ₅₀₀	DθDZ ₈₅₀₋₅₀₀	θ _{TOP}	θ _{BASE}	θ _{2M}
DT _{INV}	1.00												
DZ _{INV}	0.34	1.00											
Z _{TOP}	-0.02	0.30	1.00										
Z _{BASE}	-0.14	-0.05	0.94	1.00									
Dθ _{850,SC}	0.55	0.32	-	-0.42	1.00								
T _{TOP}	0.33	0.10	-	-0.82	0.48	1.00							
T _{BASE}	-0.06	-0.03	-	-0.81	0.28	0.92	1.00						
T ₈₅₀	0.40	0.21	-	-0.66	0.65	0.91	0.80	1.00					
T ₅₀₀	0.15	0.13	-	-0.27	0.32	0.43	0.39	0.46	1.00				
DθDZ ₈₅₀₋₅₀₀	-0.32	-0.13	0.46	0.53	-0.48	-	-0.60	-	0.22	1.00			
θ _{TOP}	0.46	0.57	0.29	0.09	0.31	0.42	0.25	0.55	0.32	-0.37	1.00		
θ _{BASE}	-0.33	-0.12	0.16	0.21	-0.18	0.25	0.49	0.30	0.22	-0.17	0.57	1.00	
θ _{2M}	0.06	0.01	-	-0.52	0.02	0.80	0.82	0.77	0.34	-0.60	0.47	0.55	1.00

Table 9. Correlation of monthly means from 1960–2007 San Diego 00Z radiosonde measurements. The monthly means were calculated using only those days when a subsidence inversion was observed in the radiosonde data. The various time series were detrended prior to calculation.

	DT _{INV}	DZ _{INV}	Z _{TOP}	Z _{BASE}	Dθ ₈₅₀	T _{TOP}	T _{BASE}	T ₈₅₀	T ₅₀₀	DθDZ ₈₅₀₋₅₀₀	θ _{TOP}	θ _{BASE}	θ _{2M}
DT _{INV}	1.00												
DZ _{INV}	0.63	1.00											
Z _{TOP}	-0.20	0.07	1.00										
Z _{BASE}	-0.39	-0.26	0.95	1.00									
Dθ _{850,SC}	0.76	0.57	-	-0.48	1.00								
T _{TOP}	0.47	0.28	-	-0.86	0.51	1.00							
T _{BASE}	0.12	0.05	-	-0.81	0.26	0.93	1.00						
T ₈₅₀	0.54	0.35	-	-0.75	0.61	0.96	0.86	1.00					
T ₅₀₀	0.25	0.23	-	-0.44	0.44	0.58	0.54	0.62	1.00				
DθDZ ₈₅₀₋₅₀₀	-0.49	-0.26	0.56	0.63	-0.44	-	-0.68	-	-	1.00			
θ _{TOP}	0.54	0.53	-	-0.29	0.46	0.70	0.56	0.79	0.50	-0.63	1.00		
θ _{BASE}	-0.34	-0.26	-	0.03	-0.23	0.38	0.57	0.41	0.31	-0.28	0.55	1.00	
θ _{2M}	0.10	0.01	-	-0.58	0.00	0.82	0.89	0.80	0.45	-0.68	0.65	0.70	1.00

There is also similar low-frequency variability between many of the inversion measures. Correlations of low-frequency subsidence inversion variability for several inversion measures are displayed in Tables 10 and 11, for Oakland and San Diego, respectively. The low frequency data was obtained by applying a five-year running mean filter through the monthly mean data. This filtering has the effect of reducing the independent number of observations to something on the order of 10 (48 years divided by 5), with correlations greater than 0.59 being significant at the 95% confidence level.

Table 10. Correlation of low-frequency subsidence inversion variability (five-year running mean filter) from 1960–2007 Oakland 00Z radiosonde measurements. The various time series were detrended prior to calculation.

	DT _{INV}	DZ _{INV}	Z _{TOP}	Z _{BASE}	Dθ ₈₅₀	T _{TOP}	T _{BASE}	T ₈₅₀	T ₅₀₀	DθDZ ₈₅₀₋₅₀₀	θ _{TOP}	θ _{BASE}	θ _{2M}
DT _{INV}	1.00												
DZ _{INV}	0.80	1.00											
Z _{TOP}	0.13	0.37	1.00										
Z _{BASE}	-0.47	-0.38	0.72	1.00									
Dθ _{850,SJV}	-0.16	0.18	0.00	-0.13	1.00								
T _{TOP}	0.24	0.14	-	-0.74	0.47	1.00							
			0.63										
T _{BASE}	-0.44	-0.39	-	-0.37	0.55	0.77	1.00						
			0.67										
T ₈₅₀	0.14	0.11	-	-0.54	0.61	0.95	0.79	1.00					
			0.46										
T ₅₀₀	0.01	0.19	0.21	0.07	0.42	0.36	0.32	0.47	1.00				
DθDZ ₈₅₀₋₅₀₀	-0.13	0.04	0.66	0.62	-0.33	-	-0.59	-	0.30	1.00			
						0.74		0.70					
θ _{TOP}	0.44	0.62	0.45	-0.02	0.57	0.41	0.09	0.56	0.63	-0.09	1.00		
θ _{BASE}	-0.80	-0.67	0.01	0.51	0.42	0.08	0.60	0.28	0.35	-0.02	0.09	1.00	
θ _{2M}	0.36	-0.03	-	-0.53	-0.29	0.67	0.38	0.57	0.14	-0.51	0.10	-0.12	1.00
			0.56										

Table 11. Correlation of low-frequency subsidence inversion variability (five-year running mean filter) from 1960–2007 San Diego 00Z radiosonde measurements. The various time series were detrended prior to calculation.

	DT _{INV}	DZ _{INV}	Z _{TOP}	Z _{BASE}	Dθ ₈₅₀	T _{TOP}	T _{BASE}	T ₈₅₀	T ₅₀₀	DθDZ ₈₅₀₋₅₀₀	θ _{TOP}	θ _{BASE}	θ _{2M}
DT _{INV}	1.00												
DZ _{INV}	0.90	1.00											
Z _{TOP}	0.18	0.43	1.00										
Z _{BASE}	-0.81	-0.74	0.30	1.00									
Dθ _{850,SC}	0.74	0.67	0.20	-0.56	1.00								
T _{TOP}	0.48	0.49	-	-0.75	0.50	1.00							
			0.32										
T _{BASE}	-0.66	-0.54	-	0.22	-0.35	0.34	1.00						
			0.47										
T ₈₅₀	0.21	0.24	-	-0.44	0.41	0.90	0.56	1.00					
			0.26										
T ₅₀₀	-0.28	-0.11	0.05	0.16	-0.05	0.27	0.53	0.57	1.00				
DθDZ ₈₅₀₋₅₀₀	-0.51	-0.34	0.31	0.59	-0.45	-	0.07	-	0.61	1.00			
						0.54		0.31					
θ _{TOP}	0.58	0.77	0.53	-0.42	0.61	0.63	-0.08	0.60	0.32	-0.19	1.00		
θ _{BASE}	-0.93	-0.80	-	0.79	-0.57	-	0.77	0.08	0.47	0.45	-	1.00	
			0.08			0.26					0.29		
θ _{2M}	-0.66	-0.56	-	0.32	-0.81	0.03	0.73	0.19	0.43	0.29	-	0.66	1.00
			0.37								0.27		

At both Oakland and San Diego, the low frequency variability of DT_{INV} and DZ_{INV} are strongly correlated. Similar correlation strengths were found for both sets of inversion measures at the daily and monthly time scales. Interestingly, the correlation between DT_{INV} and T_{BASE} is much stronger for low-frequency variability than it is on either daily or monthly time scales at both sites. Conversely, correlations between DT_{INV} and T₈₅₀ are much stronger on the daily and monthly time scales. This may imply that changes in surface-based processes over the length of the historical data may play a significant role in the low-frequency variability of DT_{INV}, while processes in the lower-to-middle atmosphere are more important for the shorter daily and monthly timescales.

Figure 13 contains time series of annual mean DT_{INV} and DZ_{INV} anomalies for radiation inversions at Oakland and San Diego. Annual means were used rather than monthly means, as there are very few radiation inversions during summer months. Additionally, only data at 12Z is plotted since very few radiation inversions are observed at 00Z (local afternoon). Similar to subsidence inversions, both the inversion strength DT_{INV} and inversion depth DZ_{INV} are decreasing over the 48-year time period examined.

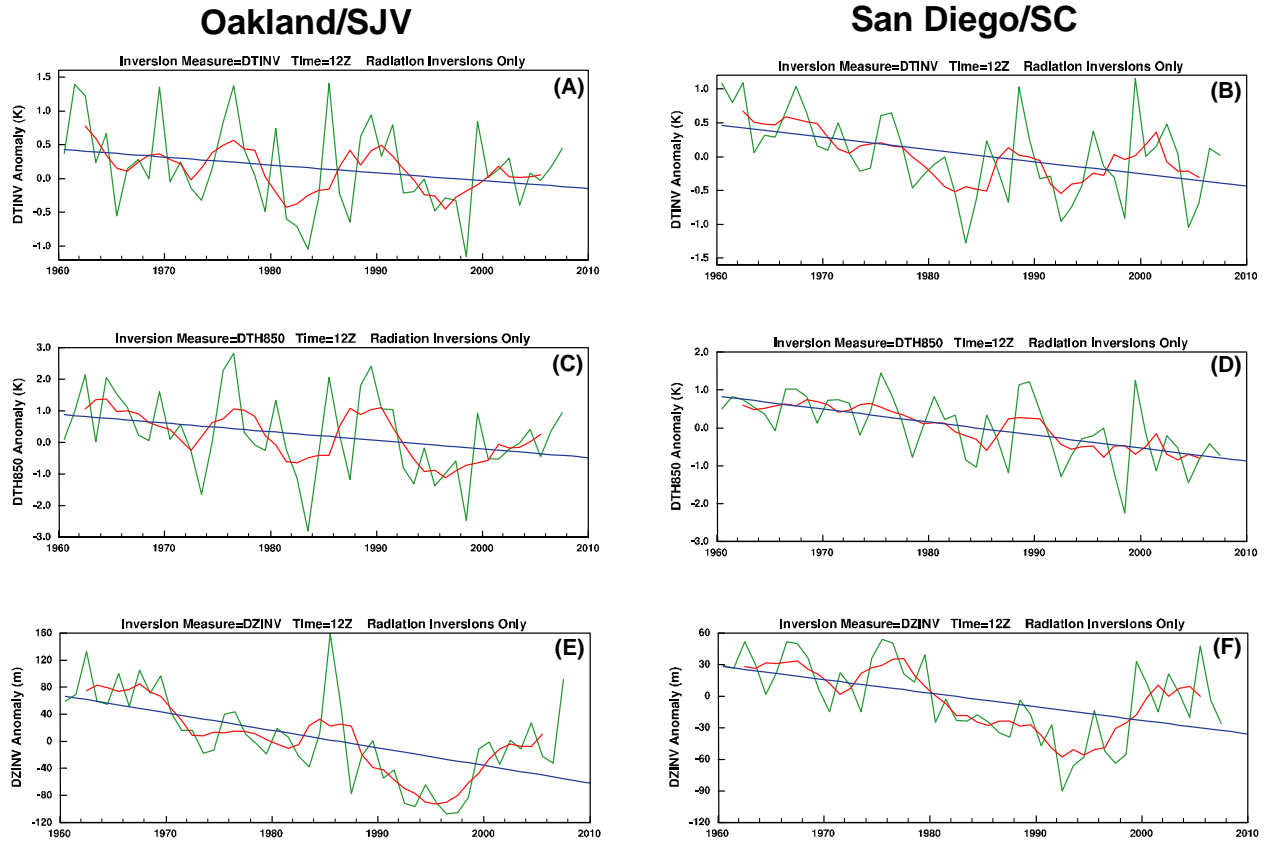


Figure 13. Time series of annual mean values of DT_{INV} (a, b), $D\theta_{850}$ (c, d), DZ_{INV} (e, f), based on radiosonde data and surface temperature measurements in the San Joaquin Valley ($D\theta_{850,SJV}$) and South Coast ($D\theta_{850,SC}$) air basins. The green line shows the annual mean data, while the red line show a five-year running mean. The straight blue lines represent a linear best fit to the data. The annual means were calculated using only days when radiation inversions were observed at 12Z.

4.4.2. Time Series of Strong and Weak Inversion Frequency

The frequency and duration of strong or weak inversion episodes could be an important consideration in air quality and health impacts. Quartile values of inversion strength are determined for each calendar month by sorting all DT_{INV} values over the 1960–2007 period. In the following analyses, to investigate effects of possible secular changes in the occurrence of strong or weak inversions, the inversion series was first detrended and later, the inversion occurrences were examined from the original (not detrended) series. Linear interpolation between the monthly values was used to calculate daily quartile values for each day of the year (monthly values were placed at midpoint of each month). Strong and weak inversions are defined as in Section 3.1. The frequency of strong inversions for a given month is the number of days when DT_{INV} exceeds Q_3 (number of days when DT_{INV} less than Q_1 for frequency of weak inversions) divided by the total number of days.

Figure 14 contains the time series of monthly frequency of strong and weak inversions at Oakland and San Diego determined from the detrended series of inversion strength. The mean

frequency of strong and weak inversions over the entire 48-year period is each 25%. However, values for individual months can vary significantly from this mean value, ranging from 0% to 77% of days within the month. There is also significant interannual and decadal variability in both strong and weak inversion frequency. The high activity inversion epoch from 1973–1977 was a period in which strong inversions occurred, in aggregate over the five-year period, 30% of the time, while the low activity inversion epoch from 1983–1987 was a period when strong inversions occurred only 19% of the time on average over that five-year period. Generally, the frequency of strong inversions varies inversely from that of weak inversions. A noteworthy exception occurred between 1995–2000, when both strong and weak inversion at 00Z increased in frequency at both locations.

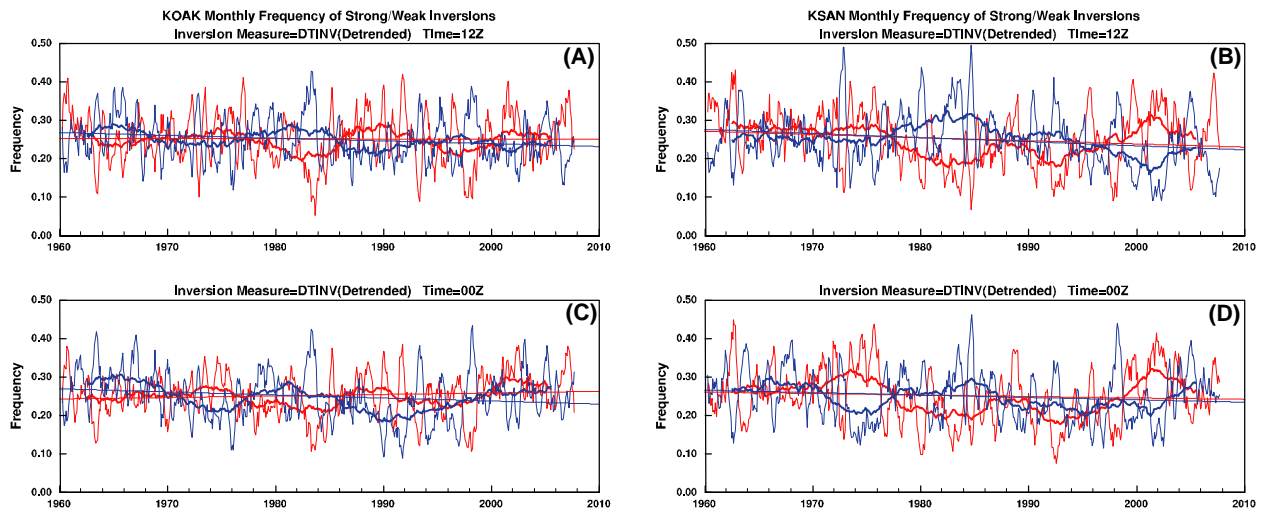


Figure 14. Time series of monthly frequency of strong and weak inversions at Oakland (a, c) and San Diego (b, d). Red curves show the frequency of strong inversions while the blue curve shows the frequency of weak inversions. The data was smoothed using a six-month running mean (thin lines) and five-year running mean (thick curves) filters. The straight lines represent a linear best fit. Strong inversions are defined when DT_{INV} exceeds the third quartile and weak inversions are defined when DT_{INV} is less than the first quartile value. Quartiles were calculated for each calendar month using detrended daily values of DT_{INV} derived from radiosonde measurements over the 1960–2007 period at each site.

Because the DT_{INV} time series were detrended prior to computing the strong/weak inversion frequencies, long-term trends in inversion strength, DT_{INV} , have no impact on the occurrence frequency of strong inversions, shown in Figure 14. As a result, any significant long-term trends in Figure 14 are due to changes in the shape of the frequency distribution of DT_{INV} . For example, if the DT_{INV} frequency distribution became broader (assume equal changes on both sides of the median) in time, this would not change the overall strength of the inversions, but would produce an increase in the frequency of strong/weak inversion occurrences. A change to a more narrow distribution would similarly not change the overall strength but would have the opposite effect in reducing the frequency of strong and weak inversions.

However, there may be long-term trends in DT_{INV} that would affect the strong/weak inversion frequency. To gauge this impact, the frequency of strong inversions was recalculated using the original non-detrended DT_{INV} time series, and Table 12 shows the number of strong inversion days per year for the first and second half of the 1960–2007 study period. At San Diego, there were about 16–20 fewer strong inversion days per year during the second half of the time period, compared to a long-term average of about 91 strong inversion days per year. The difference at Oakland was not as large, with about 5–8 fewer strong inversion days per year during the second half of the period.

Table 12. Average number of strong inversion days per year based on time series of DT_{INV} that was not detrended. Values are given for the first and second half of the period.

	1960–1983	1984–2007
KSAN 12Z	99.4	83.1
KSAN 00Z	101.0	81.5
KOAK 12Z	93.7	88.9
KOAK 00Z	95.2	87.3

Differences in the number of strong inversions are even more apparent when shorter time periods are examined. For example, at San Diego there were on average 110 strong inversions per year during the five-year period 1973–1977. During 1983–1987 there were only 71 strong inversions per year, or a reduction, relative to the high activity 1973–1977 period, of 39 strong inversions per year. These differences illustrate that while there are inversions on most days in California, low-frequency variability in inversion strength (along with other inversion characteristics) is an important feature of the environment.

4.4.3. Persistence of Strong and Weak Inversions

To understand how strong or weak inversions align in strings of days, the daily quartile values calculated above in Section 4.4.2 were used to examine the persistence of inversions. In this case, inversions are measured by the inversion strength DT_{INV} . Inversion persistence was investigated for the warm season (June–September) and for the cold season (Dec–March) using the persistence value (PV) described in Section 3.2. A value of PV_k , where k is the designated quartile, was calculated for each day in the 1960–2007 record. Average values of PV_k were obtained for both the warm and cold seasons.

Average values of PV for each quartile, shown in Table 13, are for the most part substantially greater than the Monte Carlo values, ranging from 0.34 to 0.78 for the warm season and from 0.35 to 0.70 for the cool season. Results are shown for both the Oakland and San Diego sites and both the warm and cold season. Inversions within quartiles 1 and 4 tend to persist longer than inversions in quartiles 2 and 3. For example, during the warm season quartile 1 and quartile 4 inversions have average PV values exceeding 0.6, while quartile 2 and quartile 3 inversions have average PV values less than 0.4. In other words, extreme inversions (both weak and strong) tend to persist more than moderate inversions. This is a general result that is applicable to both warm and cold seasons, both sites, and both the 00Z and the 12Z radiosonde launch time.

Table 13. Average value of persistence parameter PV

Designated Quartile	San Diego 12Z	San Diego 00Z	Oakland 12Z	Oakland 00Z
Warm Season				
1	0.63	0.52	0.70	0.59
2	0.41	0.39	0.41	0.34
3	0.41	0.38	0.44	0.42
4	0.67	0.64	0.78	0.64
Cold Season				
1	0.54	0.42	0.47	0.43
2	0.38	0.38	0.36	0.39
3	0.38	0.35	0.37	0.35
4	0.70	0.49	0.67	0.51

To cast inversion persistence in a slightly different measure, consider how many of all of the strong inversion cases occur in strings of two days or more. The distribution at 00Z shows that 80% and 77% of the strong summer inversions and 66% and 62% of the strong winter inversions, at Oakland and San Diego respectively, are clustered into events lasting two days or longer.

Inversion persistence tends to be stronger during the warm season than the cool season. This seasonality may be related to the more frequent synoptic events during the cold season, which reduce 850 hPa temperature through upward motion and cold vertical temperature advection. Stronger surface wind speeds during synoptic events may also increase the turbulence in the boundary layer and tend to weaken or eliminate nighttime surface temperature inversions. Inversions occurring in the early morning (12Z) also tend to be slightly more persistent than those measured in the mid-afternoon (00Z). This may be due to the multi-day tendencies of strong or weak radiation inversions that occur primarily in the early morning hours and are nearly absent in the mid-afternoon. The radiosonde sites at Oakland and San Diego have roughly the same level of inversion persistence. While Oakland is more poleward and subject to more frequent synoptic events, both locations are dominated by marine influences that could explain some of the similar characteristics.

5.0 Summary and Conclusions

From five decades of radiosonde records at Oakland and San Diego and associated observational data, the structure and variability of low-level temperature inversions in California has been considered.

The California locale, under the influence of the subsiding North Pacific High air mass, is a productive environment for low-level inversions. Low-level inversions are nearly ubiquitous, with some form of low-level inversion nearly always present at both Oakland and San Diego.

Two measures of inversions, one directly from radiosonde profiles and one from radiosonde upper air temperature combined with surface temperature observations, provide a consistent picture of the nature of inversions in the region. On average, inversions are strongest and most frequent in summer. They are still often present in winter, although on average not as strong or as frequently occurring. Shallow (base < 50 m) radiation inversions occur at night about 30%–40% of the time and break down during the day. During the day, deeper subsidence inversions were found about 60%–70% of the time during winter, while in summer they were a nearly constant feature (> 99%).

Subsidence inversions vary in several important ways, including altitude of base, top and strength of temperature difference across the inversion. Most inversion measures, including DT_{INV} and DZ_{INV} possess a strong seasonal cycle, in both magnitude and variability.

Inversions tend to occur in spells, as 73% of the strong inversions at the two primary locations (San Diego and Oakland) occurred during spells of two days or longer. These multi-day episodes are set up by larger-scale atmospheric conditions. Strong and weak inversion situations tend to persist longer than do moderate inversions, presumably in response to the lifecycle of synoptic patterns and possibly also affected by persistent influences from the Earth's surface.

Inversions at Oakland and San Diego tend to vary similarly on synoptic and longer time scales. These variations are quite strong and important – a high inversion month may contain up to 24 days having strong inversions, while a low inversion month may be without any strong inversion days. The temperature change within the inversion during strong inversion episodes is markedly larger than that when low inversions prevail – the temperature difference ($DT_{INV} = T_{TOP} - T_{BASE}$) during strong inversions at San Diego typically exceeds 10°C (18°F) in summer and 7.5°C (13.5°F) in winter, while during weak inversions it is typically less than 6°C (10.8°F) in summer and 2.5°C (4.5°F) in winter. Strong inversions are usually thicker, with an average inversion thickness of 610 m in summer and 370 m in winter, and weak inversions are usually thinner, with an average inversion thickness of 420 m in summer and 180 m in winter. Comparable differences are found at Oakland. These variations are crucial in creating conditions more or less susceptible to bad air quality in California's problem air basins. For example, the monthly frequency of strong inversions at San Diego is correlated with ozone concentration at $R=0.42$, and with sulfate particular matter at $R=0.61$ (both of these correlations exceed the 99% confidence level).

This spatial coherence of the strength and other properties of low-level inversions in California air basins are quite strongly determined by larger-scale atmospheric circulation conditions. Strong inversions result when anomalously high pressure is present over California, while anomalously low pressure is associated with weak inversions. The location of the center of these anomalous pressure systems may have important regional implications as well; strong/weak inversions at a particular location appear more likely when the pressure center is not directly overhead (i.e., the sounding location is on the flank of a nearby anomalously high or low pressure).

At subseasonal time scales, the primary driver of temperature inversions are changes in 850 hPa temperature. Surface temperature changes generally follow 850 hPa temperature changes and thus act to mute inversion strength. Variations in 850 hPa temperature are predominantly produced by variations in temperature advection. Specifically, 850 hPa temperature increases when warm vertical temperature advection outweighs cold horizontal temperature advection. This usually is caused by an increase in subsidence, but a weakening of cold horizontal advection also contributes. At seasonal and longer time scales, surface and radiative processes may contribute more strongly to changes in inversion strength.

While there are inversions of varying intensity and structure, on most days in California, low-frequency variability in inversion strength (along with other inversion characteristics) is a feature of the historical record that may have important implications for future changes. The frequency of occurrence of strong inversions varies on interannual to decadal time scales. For example, at San Diego there were periods of high activity during 1973–1977 with 110 strong inversions per year and periods of low activity during 1983–1987 with only 71 strong inversions per year. This variability is associated, to some extent, with the variability of sea surface temperature (SST) along the California coast, in the sense that periods with warmer than average SST tend to have weaker, thinner inversions and periods with cooler SST tend to have stronger, thicker inversions. The composite geopotential height anomalies for strong and weak inversions quite clearly indicate that the inversion structure is driving the same changes in atmospheric circulation and synoptic patterns that characterize these warm or cool ocean spells. These links to SST carry through to interannual and interdecadal time scales, with consistent links to the El Niño/Southern Oscillation (ENSO) and to the Pacific Decadal Oscillation (PDO). The warm and cool phases, respectively, of ENSO and PDO feature somewhat similar patterns of SST along the California coast. There is a weak association to ENSO, in the sense that warm ENSO events tend to contain fewer strong inversions. Over decadal time scales, the structure of inversions in California is linked to the Pacific Decadal Oscillation (PDO), wherein stronger and thicker inversions occur with the cool phase (relatively cool SST in the eastern Pacific off of North America) of the PDO, and vice versa. The correlations between inversion measures and the PDO are stronger at San Diego compared to Oakland.

Moreover, there are intriguing long period changes in the inversion structure—the radiosonde records and associated observational data reveal a rich set of interlinked changes between now and the 1960s (see Table 5):

- Inversion top has lowered over time about 20–60 m, with the largest changes at 12Z.
- Inversion base has risen by about 60–90 m at 00Z (changes at 12Z are inconclusive).
- Temperature of inversion base has risen over time approximately 0.9 K–1.3 K (1.6°F–2.3°F).
- Temperature of the inversion top has also risen, but not as much as the inversion base temperature.
- Overall inversion strength, as measured by the T_{TOP} minus T_{BASE} , has decreased by 0.5 K–0.6 K (0.9°F–1.1°F), amounting to declines of about 8%–16% at Oakland and San Diego.

- Lapse rate of the overlying lower-middle troposphere has increased (more stable).
- A reduction in the number of days with strong inversions, amounting to about a 6% decrease at Oakland and about a 20% decrease at San Diego.

It is possible that the changes in inversion structure and DT_{INV} and $D\theta_{850}$ inversion strength measures may have been affected by instrumental changes in radiosondes or by changes in the processing and sampling of the radiosondes over the period of record. Changes in surface conditions or surface temperature sampling could also introduce spurious changes in inversion characteristics. However, a number of analyses of the primary radiosonde records at San Diego and Oakland indicate that the changes in frequency, strength, and vertical structure of inversions cannot be attributed solely to instrumental or data processing changes. Besides the evidence presented, a number of additional analyses (not shown here) were conducted. In these new additional tests, the radiosonde observations were resampled at a lesser number of standard levels in order to remove possible effects from changes in the vertical resolution of the temperature profile. The additional results confirmed the original findings—they yielded, qualitatively, the same trends that were obtained from the original radiosonde observations. Nonetheless, additional work is needed to address the uncertainties in these trends to determine more definitively if they have been affected by procedural or instrumentation changes in the radiosonde record.

Three adjusted radiosonde data sets with independent methods for correcting inhomogeneities produce decreasing trends in $D\theta_{850,SC}$ that are close to the value of the decreasing trend in the original data. Trends for Oakland and the SJV are more uncertain, however, since the two available adjusted radiosonde data sets produce trends that are respectively more positive and more negative than the original trend. They indicate that the wintertime $D\theta_{850,SJV}$ trend was near-zero or decreasing, and that the summertime $D\theta_{850,SJV}$ trend that was near-zero or increasing.

Our present conclusion is that there is a substantial portion of the changes in inversions characteristics that are not simply artifacts of changes in measurement and data processing. If this is the case, these changes are likely related to change in processes that are associated with larger-scale atmospheric circulation changes—this is evidenced by commensurate trends of the temperature and the height of the top of the inversion. However, there have also been important trends at the base of the inversion—warmer temperatures and higher inversion base—that are linked to changes in surface temperature and possibly other surface characteristics. Novakov et al. (2008) suggest that a decrease in black carbon aerosol concentrations since 1990 have led to increased surface temperatures by allowing more solar radiation to be transmitted through the atmosphere to be absorbed at the surface. The surface temperature increase combined with reduced solar absorption in the atmosphere would, if occurring above the boundary layer, act to weaken temperature inversions. Whether these are predominately effects of changes in larger-scale atmospheric circulation or whether they are also affected by local surface influences that affect the temperature near the surface and the flux of heat and other properties into the boundary layer is still not understood. More work is needed to understand how these processes have affected, historically, low-level temperature inversions in California. Because these processes may change as climate changes, it is important

to understand them in order to better understand if they could alter inversion structure or occurrences in the future.

6.0 References

- Bonfils, C., P. Duffy, B. Santer, T. Wigley, D. B. Lobell, T. J. Phillips, and C. Doutriaux. 2007. "Identification of external influences on temperatures in California." *Clim. Ch.* 87:43–55.
- Dabdub, D., L. L. DeHaan, and J. H. Seinfeld. 1999. "Analysis of ozone in the San Joaquin Valley of California." *Atmos. Environ.* 33:2501–2514.
- Cayan, D. R., E. P. Maurer, M. D. Dettinger, M. Tyree, and K. Hayhoe. 2008. "Climate Change Scenarios for the California Region." *Climatic Change*, published online, January 26, 2008, doi:10.1007/s10584-007-9377-6.
- Duffy, P. B., R. W. Arritt, J. Coquard, W. Gutowski, J. Han, J. Iorio, J. Kim, I.-R. Leung, J. Roads, and E. Zeledon. 2006. "Simulations of present and future climates in the western United States with four nested regional climate models." *J. Climate* 19:873–895.
- Ferreria, S. R., and E. M. Shipp. 2005. *Historical meteorological analysis in support of the 2003 San Joaquin Valley PM10 state implementation plan*. Final report, California Air Resources Board. Available at www.arb.ca.gov/airways/CRPAQS/DA/met/HistoricalMet--2003PM10SIP.pdf.
- Free, M., D. J. Seidel, J. K. Angell, J. Lanzante, I. Durre, and T. C. Peterson. 2005. Radiosonde Atmospheric Temperature Products for Assessing Climate (RATPAC): A new data set of large-area anomaly time series. *J. Geophys. Res.* 110: D22101, doi:10.1029/2005JD0006169.
- Gaffen, D. J. 1994. "Temporal inhomogeneities in radiosonde temperature records." *J. Geophys. Res.* 99:3667–3676.
- Haimberger, L. 2005. Homogenization of radiosonde temperature time series using ERA-40 analysis feedback information. *ERA-40 Project Report Series No. 23*. European Centre for Medium Range Weather Forecasts, Reading, UK.
- Hogrefe, C., B. Lynn, K. Civerolo, J. Y. Ku, J. Rosenthal, C. Rosenzweig, R. Goldberg, S. Gaffin, K. Knowlton, and P. L. Kinney. 2004. "Simulating changes in regional air pollution over the eastern United States due to changes in global and regional climate and emissions." *J. Geophys. Res.* 109: D22301, doi:10.1029/2004JD004690.
- Kalnay, E, M. Kanamitsu, et al. 1996. "The NCEP/NCAR 40-year reanalysis project." *Bull. Amer. Meteor. Soc.* 77(3): 437–471.
- Kanamitsu, M., and H. Kanamaru. 2007. 57-Year California Reanalysis Downscaling at 10km (CaRD10) Part I. System Detail and Validation with Observations. Submitted for publication in *Journal of Climate*.

- Kanamaru, H., and M. Kanamitsu. 2007. 57-Year California Reanalysis Downscaling at 10km (CaRD10) Part II. Comparison with North American Regional Reanalysis. Submitted for publication in *Journal of Climate*.
- Lu, R., and R. P. Turco. 1994. "Air pollutant transport in a coastal environment. Part I: Two-dimensional simulations of sea-breeze and mountain effects." *J. Atmos. Sci.* 51: 2285–2308.
- Mahmud, A., M. Tyree, D. Cayan, N. Motallebi, and M. J. Kleeman. 2008. "Statistical downscaling of climate change impacts on ozone concentrations in California." *J. Geophys. Res.* 113, D21103, doi:10.1029/2007JD009534.
- Mesinger, F., et al. 2006. "North American regional reanalysis." *Bull. Amer. Meteor. Soc.* 87(3): 343–360.
- Mickley, L. J., D. J. Jacob, B. D. Field, and D. Rind. 2004. "Effects of future climate change on regional air pollution episodes in the United States." *Geophys. Res. Lett.* 31: L24103, doi 10.1029/2004GL021216.
- Neiburger, M. 1969. "The role of meteorology in the study and control of air pollution." *Bull. Amer. Meteor. Soc.* 50:957–965.
- Novakov, T., T. W. Kirchstetter, S. Menon, and J. Aguiar. 2008. "Response of California temperature to regional anthropogenic aerosol changes." *Geophys. Res. Lett.* 35: L19808, doi:10.1029/2008GL034894.
- Peterson, T. C., and R. S. Vose. 1997. "An overview of the Global Historical Climatology Network Temperature Database." *Bull. Amer. Meteor. Soc.* 78:2837–2849.
- Reynolds, R. W., N. A. Rayner, T. M. Smith, D. C. Stokes, and W. Wang. 2002. "An improved in situ and satellite SST analysis for climate." *J. Climate* 15:1609–1625.
- Schwartz, B. E., and M. Govett. 1992. A hydrostatically consistent North American radiosonde data base at the Forecast Systems Laboratory, 1946–present. NOAA Technical Memorandum ERL FSL-4. Available online at: <http://raob.fsl.noaa.gov/intl/radiosonde.pdf>.
- Snyder, M. A., J. L. Bell, L. C. Sloan, P. B. Duffy, and B. Govindasamy. 2002. "Climate responses to a doubling of atmospheric carbon dioxide for a climatically vulnerable region." *Geophys. Res. Lett.* 29(11): 1514, doi:10.1029/2001GL014431.
- Steiner, A. L., S. Tonse, R. C. Cohen, A. H. Goldstein, and R. A. Harley. 2006. "Influence of future climate and emissions on regional air quality in California." *J. Geophys. Res.* 111: D18303, doi:10.1029/2005JD006935.
- Tennekes, H. 1973. "A model for the dynamics of the inversion above a convective boundary layer." *J. Atmos. Sci.* 30:558–567.

- Thorne, P. W., D. E. Parker, S. F. B. Tett, P. D. Jones, M. McCarthy, H. Coleman, and P. Brohan. 2005. "Revisiting radiosonde upper air temperatures from 1958 to 2002." *J. Geophys. Res.* 110: D18105, doi:10.1029/2004JD005753.
- Wakimoto, R. M. 1987. "The Catalina Eddy and its effect on pollution over Southern California." *Mon. Wea. Rev.* 115:837–855.
- Watson, J. G., and J. C. Chow. 2002. "A wintertime PM_{2.5} episode at the Fresno, CA, supersite." *Atmos. Environ.* 36:465–475.
- Zhang, Y., J. M. Wallace, and D. S. Battisti. 1997. "ENSO-like interdecadal variability: 1900–93." *J. Climate* 10:1004–1020.

7.0 Glossary

00Z	0000 Hours Universal Coordinated Time
12Z	1200 Hours Universal Coordinated Time
θ_{850}	The potential temperature at 850 hectopascals
θ_{2M}	The potential temperature at two meters above the ground
CaRD10	California Reanalysis Downscaling at 10 km
$D\theta_{850}$	The potential temperature difference between 850 hectopascals and the surface
DT_{INV}	the temperature difference across the inversion
DZ_{INV}	the depth of the inversion
ENSO	El Niño/Southern Oscillation
ESRL	Earth System Research Laboratory
GCM	Global Climate Model
GHCN2	Global Historical Climatology Network, version 2
HadAT2	Hadley Center radiosonde data set
hPa	hectopascals
LT	local time
NCEP	National Centers for Environmental Prediction
NOAA	National Oceanic and Atmospheric Administration
PDO	Pacific Decadal Oscillation
PST	Pacific Standard Time

PV	persistence value
Q1, Q3	first quartile, third quartile
RAOBCORE	RAdiosonde OBservation CORrection using REanalyses
RATPAC	RAdiosonde Atmospheric Temperature Products for Assessing Climate
RSM	Regional Spectral Model
SJV	San Joaquin Valley
SC	South Coast
SST	sea surface temperature
T _{2m}	The temperature at two meters above the surface
T _{BASE}	the temperature at the base of the inversion
T _{max}	maximum temperature
T _{min}	minimum temperature
T _{TOP}	the temperature at the top of the inversion
UTC	coordinated universal time
Z _{BASE}	height of the base of the inversion
Z _{TOP}	the height of the top of the inversion

